



CHORUS

This is the accepted manuscript made available via CHORUS. The article has been published as:

Thermal plasmons controlled by different thermal-convolution paths in tunable extrinsic Dirac structures

Andrii Iurov, Godfrey Gumbs, Danhong Huang, and Ganesh Balakrishnan

Phys. Rev. B **96**, 245403 — Published 6 December 2017

DOI: [10.1103/PhysRevB.96.245403](https://doi.org/10.1103/PhysRevB.96.245403)

Thermal plasmons controlled by different thermal-convolution paths in tunable extrinsic Dirac structures

Andrii Iurov^{1*}, Godfrey Gumbs^{2,3}, Danhong Huang^{4,1}, and Ganesh Balakrishnan¹

¹*Center for High Technology Materials, University of New Mexico,
1313 Goddard SE, Albuquerque, NM, 87106, USA*

²*Department of Physics and Astronomy, Hunter College of the City
University of New York, 695 Park Avenue, New York, NY 10065, USA*

³*Donostia International Physics Center (DIPC),*

P de Manuel Lardizabal, 4, 20018 San Sebastian, Basque Country, Spain

⁴*Air Force Research Laboratory, Space Vehicles Directorate, Kirtland Air Force Base, NM 87117, USA*

Analytic expressions for chemical potentials without any approximations are derived for all types of extrinsic (doped) gapped Dirac-cone materials including gapped graphene, silicene, germanene and single-layer transition metal dichalcogenides. In setting up our derivations, a reliable piecewise-linear model has been established for calculating the density-of-states in molybdenum disulfide, showing good agreement with previously obtained numerical results. For spin- and valley-resolved band structures, a decrease of chemical potential with increasing temperature is found as a result of enhanced thermal populations of an upper subband. Due to the broken symmetry with respect to electron and hole states in MoS₂, the chemical potential is shown to cross a zero-energy point at sufficiently high temperatures. It is important to mention that the chemical potential at a fixed temperature can still be tuned by varying doping density and band structure of a system with an external electric or strain field. Since a thermal-convolution path (or a chemical-potential-dependent response function for the thermal convolution of fermions) starting from zero temperature must be selected in advance before obtaining finite-temperature properties of any collective quantities, e.g., polarizability, plasmon modes and damping, a control of their thermal dependence within a certain temperature range is expected for field-tunable extrinsic gapped Dirac-cone materials.

PACS numbers: 73.21.-b, 73.63.-b, 71.45.Gm, 73.20.Mf

I. INTRODUCTION

Despite the fact that the microscopic properties of various low-dimensional materials have been meticulously examined over a fairly long period of time,^{1,2} the only successful fabrication of graphene in 2004^{3,4} stimulated an intriguingly new research effort devoted to the study of atomically thin two-dimensional (2D) materials. In particular, it was by virtue of its unique, yet unexpected, massless Dirac electronic properties that led to high mobility (200,000 cm²/V·s) and ballistic transport properties.⁵⁻⁷ At the corners of the first Brillouin zone, referred to as K and K' points, there is no energy band gap and the dispersions represent a linear Dirac cone structure. Due to the existence of such an energy spectrum, opening a sufficiently large and tunable energy gap in graphene has become an important issue in order to enable electron confinement. Researchers tried to achieve this by adjoining a variety of insulating substrates⁸⁻¹¹ or even expose graphene to circularly-polarized radiation.¹² In finite-width nanoribbons, their energy band structure and gap are modified by the type of insulating ‘cousin’ that is introduced.¹³⁻¹⁵

In order to create a truly tunable band gap, one must use a material with large spin-orbit coupling or a buckled structure. In this regard, silicene, a 2D silicon structure, was deemed a good candidate. Single-monolayer Si possesses a buckled structure simply because of the larger ionic size of silicon compared to carbon. This results in a large spin-orbit band gap of 1.55 meV and the possibility to modify its energy spectrum by applying an external perpendicular electric field¹⁶⁻¹⁸. These properties make it display an experimentally realizable Kane-Mele type of quantum spin Hall effect, or a topological insulator state, because of the existence of time-reversal symmetry.^{19,20} Unlike graphene, the band structure of silicene and its nanoribbons²¹⁻²³ directly depend on spin and valley indices which lead to plenty of nanoelectronic, valleytronic and spintronic applications.

Germanene, the most recently discovered and fabricated member of atomically thin buckled 2D honeycomb lattices,²⁴⁻²⁹ demonstrates substantially larger Fermi velocities and a band gap of 20 – 90 meV. Grown by molecular beam epitaxy³⁰ and investigated with x-ray absorption spectroscopy, Ge layers demonstrated satisfactory agreement between the experimentally obtained and theoretically predicted results for its inter-atomic distance.

* Corresponding author email: aiurov@unm.edu

Another important class of innovative 2D materials is represented by direct-bandgap transition metal dichalcogenides, or TMDC's. Their chemical makeup consists of a transition metal atom M , such as molybdenum or tungsten, and two identical chalcogens C , i.e., sulfur, selenium or tellurium. Symbolically, TMDC's are described as MC_2 . In our consideration, we focus on MoS_2 due to it being the most studied representative. This material exhibits a semiconductor band structure with a very large direct gap of 1.78 eV , in contrast to its bulk states with an indirect gap of 1.3 eV , and substantial spin-orbit coupling.³¹ Strictly speaking, MoS_2 is not a Dirac material since the mass terms play a crucial role in its energy dispersions. However, its low-energy Hamiltonian contains a $t_0 a_0 \boldsymbol{\Sigma} \cdot \mathbf{k}$ term, which corresponds to the linear Dirac-cone dispersion.

An effective two-band continuum model and a lattice Hamiltonian³² using the tight-binding model can account for the hybridization of the d orbitals of Mo and the p orbitals of S atoms. It provides an adequate description for its low-energy band structure and predicts a large spin-orbit splitting.³³ Due to the breaking of inversion symmetry and spin-orbit coupling, spin and valley physics is observed in all group-IV dichalcogenides, including MoS_2 .³⁴ The low-energy states of such systems are no longer massive Dirac fermions since there is a difference between electron and hole masses as well as trigonal warping effects.³⁵ Strain engineering, used to tune optical and electronic properties of conventional semiconductors, has also been applied to MoS_2 , and its modified band structure has been theoretically calculated.³⁶ These unique electronic properties of a single-layer MoS_2 were later employed to create high-performance transistors operating at room temperature.³⁷ Such electronic models and effective Hamiltonian have also been used to investigate the collective properties of TMDC's³⁸ and their influence on the bandgap transition.³⁹ In optoelectronics, the band structure, spin and valley properties of MoS_2 could be tuned successfully by an off-resonant dressing field.⁴⁰

Current many-body and quantum-field theory methods in condensed matter physics^{41,42} have provided useful techniques to understand the electronic and transport properties of low-dimensional solids, including diverse buckled honeycomb materials.⁴³⁻⁴⁵ In most of these theories, we find the *dynamical polarization function*, or polarizability, to be the mainstay and fundamental quantity in describing the screening of an external potential by interacting electrons.^{38,46-49} In addition, the dynamic polarization function plays a key role in calculating plasmon excitations, due to charge-density oscillations, which occur in metals and doped semiconductors with free electrons. Specifically, the plasmon dispersion relations, along with their lifetimes, have been investigated theoretically for a wide range of 2D Dirac systems.^{47,50-55} The interest in graphene plasmons is due in part to the fact that these excitations have no classical counterpart.⁵⁶ Moreover, there has been a considerable experimental effort for investigating graphene plasmons, gate-tuning, infrared nano-imaging and confinement.⁵⁷⁻⁶¹ Graphene plasmonic resonances and instability at various wavelengths could be used for photodetectors in the terahertz-frequency range.⁶² Furthermore, all these techniques could be successfully leveraged to the recently fabricated materials, as discussed in the present work.

Plasmonic applications, on the other hand, are largely based on *nanoscale hybrid systems*, in which graphene plasmons are coupled to surface-plasmon excitations in metals. Technology has come a long way in combining graphene with prefabricated plasmonic nanoarrays and metamaterials to construct plasmonics-based tunable hybrid optical devices.⁶³ Therefore, accurate knowledge of plasmon-mode dispersions in graphene interfaced with metallic substrates becomes crucial. Graphene-metal contacts are important components for all such optoelectronic devices. Consequently, exploration of plasmon modes at these metallic interfaces becomes a mandatory step toward fabricating prototype devices. High-resolution electron-energy-loss spectroscopy (EELS) has been employed to investigate plasmon excitations at the surface of Bi_2Se_3 to disclose the interplay between surface and Dirac plasmons in topological insulators⁶⁴. Plasmons, their behavior, dispersions, quenching and environmental effects, have been studied thoroughly in epitaxial graphene, air-exposed graphene- Ru contacts, graphene on Pt_3Ni (111), and graphene grown on Cu (111) foils.⁶⁵⁻⁶⁹

In all cases under investigation, we need to distinguish between *extrinsic* materials, i.e., a sample initially doped at zero temperature $T = 0$, and *intrinsic* materials with zero Fermi energy and a completely empty conduction band. In the latter case, both the plasmon excitations and electrical conductivity are suppressed at $T = 0$ due to the absence of free electrons. At a finite T , on the other hand, the conduction band could still be partially populated by thermally-excited electrons from a valence band.^{70,71} For graphene with a zero bandgap, the thermally-excited carrier density n_0 is scaled as $n_0 \simeq T^2$ and the plasmon frequency Ω_{pl} is on the order of $\Omega_{pl} \simeq qT$.

The properties of intrinsic finite- T plasmon excitations have been examined systematically for various materials including silicene.⁷² In contrast, extrinsic or doped structures at finite T suffer from a difficulty to obtain an analytical and accurate expression for the T -dependent chemical potential $\mu(T)$, i.e., the selection of a thermal-convolution path or equally a $\mu(T)$ -dependent response function for the thermal convolution of fermions. It is known that $\mu(T)$ decreases with increasing T , and its value could be found from carrier-density conservation^{70,73}. Our main objective here is to obtain a set of non-integral, transcendental equations for a wide class of Dirac gapped materials with linear density-of-states (DOS), i.e., gapped graphene, silicene, germanene and TMDC's at arbitrary temperatures and densities. In

this way, many important physical quantities at finite temperatures, such as the dynamical polarization function, can be easily calculated by using a thermal-convolution scheme.

The range of temperature considered here is physically limited by the assumption of a linear or gapped Dirac cone for filling doped electrons to high conduction-band energies. Deviations from the Dirac cone are found for energies as high as 0.5 eV ,^{74,75} leading to various effects on plasmons, e.g., anisotropy, splitting and the existence of an additional acoustic plasmon branch.^{76,77} However, such high energies are far from the thermal-energy range given by $k_B T \sim \mu(T=0) \equiv E_F$ (E_F is the Fermi energy). In our current calculations for silicene, the energy is in units of $E_0 = 6.28\text{ meV}$ while the wave-number is in units of $k_0 = 1.77 \cdot 10^5\text{ cm}^{-1}$. However, for MoS₂, due to its significant energy bandgap, the energy units is chosen $E_0^{(1)} = 54.6\text{ meV}$, which corresponds to a larger electron density 10^{12} cm^{-2} .

Ref. [78] is devoted to investigation of the plasmon hybridization in silicene using time-dependent density-functional theory in the random-phase approximation for both intrinsic and extrinsic types of materials, which is especially relevant to our work. Two intrinsic plasmon interband modes have been reported at $\hbar\omega > 1.5\text{ eV}$, i.e., a hybridized π plasmon, which appears due to sp^2 and sp^3 hybridization specifically in silicene, and a stronger conventional π - σ plasmon. For $\hbar\omega < 1\text{ eV}$, two extrinsic intraband modes have been found, one of which shows strong anisotropy.

We note that chemically doped graphene might boost plasmon decay rates due to additional activated scattering mechanisms. It has been determined from the first principles that monolayer and bilayer graphene that are doped with alkali and alkaline earth metals exhibited new damping channels in the presence of both in-plane dopant and out-of-plane graphene lattice vibrations, as well as electron transitions between localized dopant and graphene electronic states.⁷⁹

At the energy $\simeq 0.2\text{ eV}$ and above, optical phonons cause a substantial effect on graphene plasmons over a wide range of temperatures. Plasmons, relaxation-time and optical conductivity might be affected by the electron-phonon coupling for given frequencies.⁸⁰ In the range from $\hbar\omega_{OP}$ and up to the interband threshold, plasmon decay channels associated with emission of an electron-hole pair by an optical phonon play an important role for the plasmon decay. However, the low-temperature effect of acoustic phonons on the plasmons in graphene for $\hbar\omega \sim E_F$ is considerably smaller. As described in Ref. [50], the total graphene dielectric function in the presence of acoustic phonons is given by $\epsilon_{tot}(q, \omega) = \epsilon_0 - V_q [\Pi^{(0)}(q, \omega) + P_{ion}(q, \omega)]$, where $\Pi^{(0)}(q, \omega)$ is our considered electron polarization function, and $P_{ion}(q, \omega) = 2E^{(0)}q^2/(\hbar\omega)^2$. While both polarizabilities have similar $\sim q^2/\omega^2$ behavior common for a two-dimensional materials, the ion polarization coefficient $E^{(0)} = 10^{-5}\text{ eV}$ is on the order of the ion confinement energy, and therefore is negligible. Such effect should also be present in silicene at about the same level due to the specified ratio of the atomic masses of Si and C.

Certainly, this situation changes at relatively high temperatures. However, all the observed and theoretically studied phonon scattering mechanisms disappear (freeze) at low temperatures (comparable with the electron Fermi energy). As a result, most existing finite-temperature transport models leave out any phonon effects.^{73,81,82} The main damping channels correspond to electron scattering due to charged impurities, intrinsic thermal phonons in graphene and dielectric losses to the substrate.⁸³

Traditionally, the T dependence of many physical quantities has been studied passively, e.g., the T dependence of a device performance is measured only after its fabrication. However, device's thermal properties can also be designed in advance (actively) for a particular T range. By tuning $\mu(T)$ around a finite T with either doping density or bandgap, the required thermal dependence can be achieved through choosing a specific thermal path, i.e., chemical potential $\mu(T)$, for the response function, $1/\{2k_B T(1 + \cosh[(\mu(T) - x)/k_B T])\}$, in a thermal convolution⁸⁴. Physically, once the $\mu(T)$ dependence becomes known, one can obtain the finite- T dynamical polarization function from Eq. (18), which is a key component for all relevant many-body calculations. These include optical absorption, electronic transport, plasmon excitations as well as electron exchange and correlation energies.⁸⁵ Here, we focus on finite- T plasmon excitations, demonstrating doping effects on modifications of plasmon-energy dispersions at intermediate T . If T becomes high, i.e., $k_B T \gg E_F$, thermal excitation of electrons will dominate over doping effects.

The rest of the paper is organized as follows. We derive the implicit analytic equations for the chemical potential at a finite T for all types of Dirac structures with linear DOS in Sec. II. In Sec. III, we calculate the finite- T dynamic polarization function which includes the single-particle-mode frequencies. These single-particle modes combine with a charge cloud to form weakly-interacting quasiparticles that oscillate collectively at a series of characteristic plasma frequencies. Here, our emphasis has been put on simple cases with gapped graphene and silicene at intermediate T for which doping still plays a crucial role. We further study *non-local*, *hybrid* plasmon modes in an open system which contains a semi-infinite conductor coupled via Coulomb interactions to an embedded doped 2D layer. Our concluding remarks and a concise discussion are presented in Sec. IV. We also provide detailed derivations of the DOS for silicene and MoS₂ in Appendix A, as well as their corresponding explicit expressions for $\mu(T)$ in Appendix B.

II. THERMAL-CONVOLUTION PATHS

The quantum natures of electrons and holes in 2D materials are maximized at $T = 0$. At finite T , however, a thermal convolution of these quantum states must be done so as to find the T dependence of electronic properties. The final stage of this thermal convolution depends on the chemical potential $\mu(T)$ of the systems under consideration, i.e., the selection of the so-called convolution path. Such convolution paths can be switched by controlling bandgaps of systems through an applied electric field or tuned by electron doping densities through a depletion gate.

In this section, we present our analytical calculations for $\mu(T)$ as a function of T . By starting from a value equivalent to the Fermi energy E_F at $T = 0$, $\mu(T)$ usually decreases with increasing T . Its specific value depends on multiple material parameters such as energy bandgaps, Fermi velocities, density of states (DOS) of electrons above and holes below the zero energy. Thus, for a conventional 2D electron gas (2DEG) with no holes, $\mu(T)$ becomes negative above a certain temperature. However, such a phenomenon does not appear in a Dirac system with a symmetry between electron and hole states. Here, we are going to provide closed-form transcendental equations for $\mu(T)$ in a number of Dirac systems, including graphene, buckled honeycomb lattices, and transition metal dichalcogenides.

A. Buckled Honeycomb Lattices

One of the most outstanding features of silicene and other buckled honeycomb lattices is the existence of two pairs of doubly-degenerate energy subbands and two inequivalent bandgaps. These include a fixed intrinsic spin-orbit gap $2\Delta_{SO}$ and a tunable sublattice-asymmetry gap Δ_z induced by a perpendicular electric field \mathcal{E}_z . For low \mathcal{E}_z , we find $\Delta_z = \mathcal{E}_z d_\perp$ (assuming $\mathcal{E}_z \geq 0$), where d_\perp is the out-of-plane displacement of a buckled lattice.

The low-energy model Hamiltonian for a buckled honeycomb lattice has been found as^{16,17}

$$\hat{\mathbb{H}}_{\xi,\sigma} = \hbar v_F (\xi k_x \hat{\tau}_x + k_y \hat{\tau}_y) \otimes \hat{\mathbb{I}}_{2 \times 2} - \xi \Delta_{SO} \hat{\Sigma}_z \otimes \hat{\tau}_z + \Delta_z \hat{\tau}_z \otimes \hat{\mathbb{I}}_{2 \times 2}, \quad (1)$$

where $\mathbf{k} = (k_x, k_y)$ is a 2D wave vector of electrons, the Fermi velocity $v_F = 0.5 \times 10^8 \text{ cm} \cdot \text{s}^{-1}$ is half of that for graphene, $\xi = \pm 1$ is the K/K' valley index, $\hat{\tau}_{x,y,z}$ and $\hat{\Sigma}_{x,y,z}$ are Pauli matrices in two different spaces, i.e., pseudospin and real spin of electrons.

After introducing a spin index $\sigma = \pm 1$, we can rewrite Eq. (1) in a block-diagonal matrix form

$$\hat{\mathbb{H}}_{\xi,\sigma} = \begin{bmatrix} -\xi\sigma\Delta_{SO} + \Delta_z & \hbar v_F(k_x - ik_y) \\ \hbar v_F(k_x + ik_y) & \xi\sigma\Delta_{SO} - \Delta_z \end{bmatrix}. \quad (2)$$

As a result, the associated energy dispersions become

$$\varepsilon_{\xi,\sigma}^\gamma(k) = \gamma \sqrt{(\xi\sigma\Delta_z - \Delta_{SO})^2 + (\hbar v_F k)^2}, \quad (3)$$

where $\gamma = \pm 1$ labels either the electron or hole state similar to graphene with a finite or zero bandgap. The dispersions in Eq. (3) represent two pairs of spin-dependent energy subbands for each valley, leading to two different bandgaps of $|\Delta_{SO} - \xi\sigma\Delta_z|$, i.e., $\Delta_< = |\Delta_{SO} - \Delta_z|$ and $\Delta_> = \Delta_{SO} + \Delta_z$. Clearly, both energy gaps depend on \mathcal{E}_z and two subbands correspond to $\xi\sigma = \pm 1$. Small or zero \mathcal{E}_z is associated with a topological insulator (TI) state with $\Delta_z < \Delta_{SO}$. Once $\Delta_{SO} = \Delta_z$ is reached, we are left with a metallic gapless state having $\Delta_< = 0$, which appears as a valley-spin polarized metal (VSPM). For even larger \mathcal{E}_z , we have $\Delta_z > \Delta_{SO}$, leading to a standard band insulator (BI) state.

Here, the DOS is defined by

$$\rho_d(\mathbb{E}) = \int \frac{d^2\mathbf{k}}{(2\pi)^2} \sum_{\gamma=\pm 1} \sum_{\xi,\sigma=\pm 1} \delta(\mathbb{E} - \varepsilon_{\xi,\sigma}^\gamma(k)), \quad (4)$$

and for silicene (see Appendix A) it is calculated explicitly as

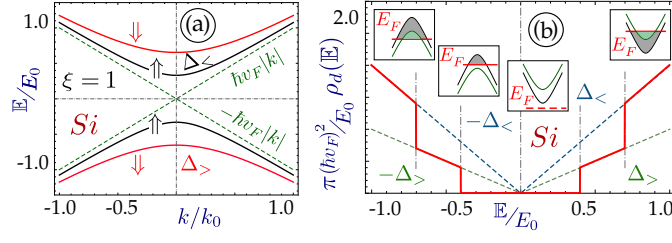


FIG. 1: (Color online) Energy dispersions in (a) and density-of-states (DOS) in (b) for silicene. Panel (a) represents low-energy dispersions around K valley ($\xi = 1$), where $\sigma = \pm 1$ relates to two inequivalent bandgaps $\Delta_<$ and $\Delta_>$. Also in (a), the linear dispersion (dashed lines), corresponding to zero bandgaps, is included for comparisons.

$$\rho_d(\mathbb{E}) = \frac{1}{\pi} \sum_{\gamma=\pm 1} \frac{\mathbb{E}}{\hbar^2 v_F^2} \sum_{i=<,>} \Theta\left(\frac{\mathbb{E}}{\gamma} - \Delta_i\right), \quad (5)$$

where $\Theta(x)$ is a unit-step function. We find from Eq. (5) that for systems sharing the same Dirac-cone characteristics with an arbitrary energy gap, the DOS is always linear, analogous to graphene. Experimentally observed linear V -shaped DOS was used to verify the Dirac-cone dispersion for germanene.⁸⁶ However, $\rho_d(\mathbb{E})$ becomes finite only above $\Delta_<$, demonstrating the importance of a bandgap.

For finite T , $\mu(T)$ of an electronic system with a fixed doping density n can be computed based on the conservation of net electrons (n_e) and holes (n_h). This yields

$$n = n_e(T) - n_h(T) = \int_0^{\infty} d\mathbb{E} \rho_d(\mathbb{E}) f_{\gamma=1}(\mathbb{E}, T) - \int_{-\infty}^0 d\mathbb{E} \rho_d(\mathbb{E}) [1 - f_{\gamma=1}(\mathbb{E}, T)], \quad (6)$$

where $f_{\gamma=1}(\mathbb{E}, T) = \{1 + \exp[(\mathbb{E} - \mu(T))/k_B T]\}^{-1}$ is the Fermi function for thermal-equilibrium electrons.

For silicene, the doping density n at $T = 0$ K can be related to E_F in a straightforward way. If only the lower subband is populated, we obtain E_F from

$$n = \frac{1}{2\pi} \frac{E_F^2 - \Delta_<^2}{\hbar^2 v_F^2}. \quad (7)$$

Alternatively, if both subbands are populated by doping at $T = 0$, then we get the relation

$$n = \frac{1}{\pi} \frac{1}{\hbar^2 v_F^2} \left[E_F^2 - \frac{1}{2} (\Delta_<^2 + \Delta_>^2) \right], \quad (8)$$

which can be applied to evaluate E_F with a fixed n . When $E_F = \Delta_>$, it gives rise to a critical density $n_c = 2\Delta_{SO}\Delta_z/\pi\hbar^2 v_F^2$ for the starting occupation of the upper subband.

For fixed n and T , $\mu(T)$ of silicene could be obtained by numerically solving the following equation^{87,88}

$$\left(\frac{\hbar v_F}{k_B T}\right)^2 n = \sum_{\gamma=\pm 1} \frac{\gamma}{\pi} \sum_{i=<,>} \left(-\text{Li}_2 \left\{ -\exp \left[\frac{\gamma \mu(T) - \Delta_i}{k_B T} \right] \right\} + \frac{\Delta_i}{k_B T} \ln \left\{ 1 + \exp \left[\frac{\gamma \mu(T) - \Delta_i}{k_B T} \right] \right\} \right), \quad (9)$$

where $\text{Li}_2(x)$ is the so-called polylogarithm function^{89,90}. Here, we derive Eq. (9) for $\mu(T)$ at arbitrary T , and E_F can be found from its solution at $T = 0$. Although this equation is *transcendental* and cannot be solved algebraically, a quasi-analytic or one-step numerical solution could be obtained easily for any T without performing an integration as described in Eq. (6). For MoS_2 , another equation for $\mu(T)$ has been derived in Appendix B.

$\mu(T)$ for silicene depends on two energy bandgaps Δ_i with $i = <, >$. Our approach, as discussed in Appendix B, remains valid for a variety of materials with a linearly energy-dependent DOS, including MoS_2 . As a special case,

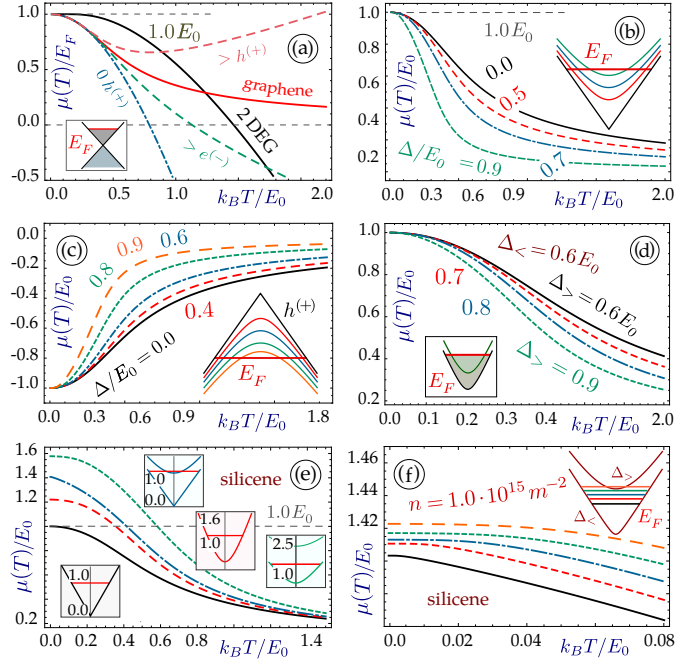


FIG. 2: (Color online) $\mu(T)$ for graphene, silicene and a 2DEG. Panel (a) presents $\mu(T)$ with fixed $E_F/E_0 = 1$ for the 2DEG (black solid curve), gapless graphene (red solid curve), graphene without holes (blue dash-dotted curve), graphene with reduced hole DOS $\rho_d^{(h)}(\mathbb{E} < 0) = \rho_d^{(e)}(\mathbb{E} > 0)/2$ (green dashed curve), and graphene with reduced electron DOS $\rho_d^{(e)}(\mathbb{E} > 0) = \rho_d^{(h)}(\mathbb{E} < 0)/2$ (orange dashed curve). Plots (b) and (c) display $\mu(T)$ for gapped graphene with fixed $E_F/E_0 = 1$ and $E_F/E_0 = -1$ for electron and hole doping, respectively, in which each curve is associated with a specific energy gap Δ_0 , as described schematically in the two insets. In (d), $\mu(T)$ of silicene is plotted with both subbands filled for fixed $E_F/E_0 = 1$, where $\Delta_{<}/E_0 = 0.6$ while $\Delta_{>}/E_0$ increases from 0.6 to 0.9 in steps of 0.1. Plot (e) presents a comparison of $\mu(T)$ with fixed $n = 1 \times 10^{11} \text{ cm}^{-2}$ for electron doping in four different cases as illustrated by four insets, including graphene with $\Delta_0 = 0$ (black solid curve); gapped graphene with $\Delta_0/E_0 = 0.7$ (red dashed curve); silicene with $\Delta_{<} = 0$, $\Delta_{>}/E_0 = 1.4$ (blue dash-dotted curve); and silicene with $\Delta_{<}/E_0 = 0.7$, $\Delta_{>}/E_0 = 2.1$ (green dashed curve). Panel (f) shows silicene $\mu(T)$ for $k_B T \ll E_F$ and $\Delta_{SO}/E_0 = 0.7$ while Δ_z/E_0 increases from 0.70 to 0.90 in steps of 0.05, where $n = 1 \times 10^{11} \text{ cm}^{-2}$ is fixed for electron doping.

Eq. (9) also describes $\mu(T)$ for gapped graphene with two degenerate subbands, i.e., $\Delta_{<} = \Delta_{>} = \Delta_0$. For gapless pristine graphene with $\Delta_0 = 0$ and $\pi n = [E_F/(\hbar v_F)]^2$, Eq. (9) is simply reduced to

$$\frac{1}{2(k_B T)^2} E_F^2 = - \sum_{\gamma=\pm 1} \gamma \text{Li}_2 \left\{ -\exp \left[\frac{\gamma \mu(T)}{k_B T} \right] \right\}. \quad (10)$$

If the temperature is low such that $k_B T \ll E_F$, Eq. (10) further reduces to those reported in Refs. [70,73,91].

All materials considered in this paper could physically be classified by their symmetries and degeneracies of energy subbands. As an example, graphene represents the simplest case with a fourfold spin and valley degeneracy for the electron and hole energy bands $\pm \sqrt{(\hbar v_F k)^2 + \Delta_0^2}$. For silicene and germanene, although their energy dispersions show full symmetry with respect to electrons and holes, they depend on spin and valley indices and are only doubly degenerate. Finally, MoS_2 displays broken symmetry between pairs of electron and hole subbands, along with subband splitting within the hole pair for different spins. Although the thermally excited electrons and holes, which are measured by $\mu(T)$, do not change the carrier conservation in Eq. (6), the broken symmetry between electron and hole subbands make them contribute differently to the modification of electronic properties.

Results for silicene energy dispersions and DOS $\rho_d(\mathbb{E})$ are presented in Fig. 1. Here, we only consider the K valley with $\xi = 1$ and two bandgaps $\Delta_{>}$ and $\Delta_{<}$ for $\sigma = \pm 1$. The spin splitting of subband pairs for electrons and holes is found significant and symmetrical but is reduced and eventually merges with the spin-degenerate linear dispersions of gapless structure at large k values. As one can see, whenever a subband is occupied, as indicated in the insets of Fig. 1(b), a step develops in $\rho_d(\mathbb{E})$. It is evident that $\rho_d(\mathbb{E})$ for both silicene and gapped graphene becomes proportional to \mathbb{E} , i.e., the DOS for Dirac materials with or without an energy gap is the same if the zero energy point is set at the gap center. In addition, since no electronic states exist inside the gap region, one requires $\rho_d(\mathbb{E}) = 0$ for $|\mathbb{E}| < \Delta_{<}/2$.

We display in Fig. 2 the calculated $\mu(T)$ for graphene and buckled honeycomb lattices, where we find their T dependence is very sensitive to the band structure when either the Fermi energy E_F in (a)-(d) or the doping density n in (e)-(f) is fixed at different values. A comparison is shown in Fig. 2(a) with fixed $E_F = E_0$ for various electron doped systems, including a 2DEG with a parabolic energy band, no hole states and a constant DOS, graphene with $\rho_d(\mathbb{E}) \sim \mathbb{E}$, as well as three *model structures*, i.e., graphene without hole states, graphene with doubly prevailing electron DOS $\rho_d(\mathbb{E} > 0) = 2\rho_d(\mathbb{E} < 0)$ or doubly prevailing hole DOS $\rho_d(\mathbb{E} < 0) = 2\rho_d(\mathbb{E} > 0)$. At low T , all $\mu(T)$ curves for gapless graphene, except for the 2DEG one, are nearly identical since holes do not play a role in this case, i.e., $1 - f_{\gamma=1}(\mathbb{E}, T) \rightarrow 0$. As T increases and becomes comparable to E_F , the thermally-excited holes are no longer negligible, which suppresses the reduction of $\mu(T)$ and prevents it from going negative for graphene. Such a hole effect is highlighted in a hole-dominating system (labelled as $> h^{(+)}$) with $\rho_d(\mathbb{E} > 0) = 2\rho_d(\mathbb{E} < 0)$, where $\mu(T)$ increases with T even above its starting value E_F . Therefore, we conclude that it is the total electron-hole symmetry, instead of the energy gap, that keeps $\mu(T)$ non-negative at high T . In the remaining panels of Fig. 2, we study $\mu(T)$ as a function of T for graphene and silicene with different band structures or gaps. In plots (b)-(d), we keep $E_F = E_0$ fixed so that the actual doped electron density n becomes smaller with a larger energy gap as can be seen from Eq.(8). Alternatively, we can fix the doping density n as in plots (e)-(f) so that the Fermi energy E_F will increase with the energy gap.

In Fig. 2, plots (b) and (c) are used to demonstrate complete reflection symmetry of $\mu(T)$ between electron and hole doping for all energy bandgaps, which is a manifestation of $\gamma = \pm 1$ symmetry in these electronic states for arbitrary T . Silicene with both subbands filled in panel (d) exhibits qualitatively similar finite- T features as those of gapped graphene in (b) for electron doping. It is clear that only gap values but not types of states (TI or BI) are relevant in determining $\mu(T)$. If E_F for silicene is set lower than but very close to the bottom of its $\Delta_>$ subband, this upper subband is expected to be thermally populated as T increases from zero, leading to an accelerated reduction of $\mu(T)$ at low T as shown by the blue dash-dotted curve in (e). For the same reason, silicene with $\Delta_< = 0$ shows a similar feature to gapped graphene at high T , where E_F is measured from the graphene zero-energy point. Furthermore, by modifying the band structure so as to populate/depopulate the upper $\Delta_>$ subband in (f), we find $\mu(T)$ develops a significant reduction with T whenever the upper subband is occupied. Therefore, either by changing band structure with a perpendicular electric field for a fixed doping density or by varying the electron doping density with a depletion gate for a fixed band structure, we are able to select different paths for thermal convolutions and tune T -dependent electronic properties along the selected convolution path, e.g., plasmon dispersion and quasiparticle lifetime⁹¹.

B. Transition Metal Dichalcogenides

In the previous discussion for silicene, $\gamma = \pm 1$ symmetry related to electron and hole states is retained. Such a symmetry, however, breaks down for MoS₂. The broken electron-hole symmetry is expected to have a profound influence on selecting paths for a thermal convolution of quantum states of electrons and holes, as well as in the T dependence of electronic properties for a given convolution path. For monolayer MoS₂, its low-energy electronic states could be effectively described by a *two-band* model Hamiltonian^{32,34,38}

$$\hat{\mathbb{H}}_d^{\xi, \sigma} = \left(\frac{1}{2} \xi \sigma \lambda_0 + \frac{\hbar^2 k^2}{4m_e} \alpha \right) \hat{\mathbb{I}}_{2 \times 2} + \left(\frac{\Delta}{2} - \frac{1}{2} \xi \sigma \lambda_0 + \frac{\hbar^2 k^2}{4m_e} \beta \right) \hat{\Sigma}_z + t_0 a_0 \hat{\Sigma}_\xi \cdot \mathbf{k}, \quad (11)$$

whose important feature includes a major gap parameter $\Delta = 1.9 eV$, which results in an actual band gap $\simeq 1.7 eV$, as well as a spin-orbit coupling parameter $\lambda_0 = 0.042 \Delta$, which represents a smaller but essential correction to the hole subband splitting and the bandgap. The energy subbands now become spin (σ) and valley (ξ) dependent due to lifting of the degeneracy. The electron hopping parameter $t_0 = 0.884 \Delta$ and the lattice constant $a_0 = 1.843 \text{ \AA}$ shape the Dirac cone term in Eq. (11) as $t_0 a_0 = 4.95 \times 10^{-29} J \cdot m$, counting up to ≈ 0.47 of $\hbar v_F$ in graphene. Next, we turn to $\sim k^2$ mass terms with $\alpha = 2.21 = 5.140 \beta$ in which m_e is the free-electron mass. The Fermi wave number $k_F = \sqrt{\pi n}$ is determined¹¹⁰ by an experimentally accessible range for electron and hole doping densities $n = 10^{10} \sim 10^{12} \text{ cm}^{-2}$, giving rise to $k_F \simeq 10^6 \sim 10^7 \text{ cm}^{-1}$. In addition, the excluded anisotropic trigonal warping term $t_1 a_0^2 (\hat{\Sigma}_\xi \cdot \mathbf{k}) \hat{\sigma}_x (\hat{\Sigma}_\xi \cdot \mathbf{k})$ in Eq. (11) is found insignificant since it is around $0.1 eV = 0.053 \Delta$ and too small to contribute to the energy dispersion of electrons.

The associated energy dispersion relation is given by $\varepsilon_{\gamma}^{\xi, \sigma}(k) = \mathbb{E}_0^{\xi, \sigma}(k) + \gamma \left\{ [\Delta_0^{\xi, \sigma}(k)]^2 + (t_0 a_0 k)^2 \right\}^{1/2}$, which is formally identical to *gapped graphene*^{38,92} but with a k -dependent gap term $\Delta_0^{\xi, \sigma}(k) = \hbar^2 k^2 \beta / (4m_e) + \Delta / 2 - \xi \sigma \lambda_0 / 2$, as well as a k -dependent band shift $\mathbb{E}_0^{\xi, \sigma}(k) = \hbar^2 k^2 \alpha / (4m_e) + \xi \sigma \lambda_0 / 2$. As a leading-order approximation, by neglecting all higher order terms $\mathcal{O}(k^4)$, we find

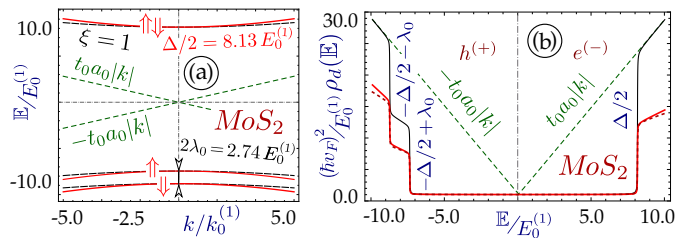


FIG. 3: (Color online) Energy dispersions and density-of-states (DOS) for molybdenum disulfide in (a) and (b). Panel (a) represents low-energy dispersions around K valley ($\xi = 1$) for MoS_2 . Linear dispersion (dashed lines), corresponding to gapless material with $\hbar v_F = a_0 t_0$, is also included for comparison. The wave-vector range in (b) is enlarged to highlight a small curvature for MoS_2 energy dispersions. Comparisons of MoS_2 results are presented for dispersions (in (a)) and DOS (in (b)), which are calculated respectively by Eq. (13) (black dashed curve in (a) and black solid curve in (b)) and by Eq. (12) (red solid curves). The exact numerical calculation for MoS_2 DOS is also displayed in (b) (wine dashed curve) as a demonstration for the accuracy of Eq. (12).

$$\varepsilon_{\gamma}^{\xi, \sigma}(k) \simeq \frac{1}{2} \xi \sigma \lambda_0 + \frac{\alpha \hbar^2}{4m_e} k^2 + \frac{\gamma}{2} \left\{ [(2t_0 a_0)^2 + (\Delta - \xi \sigma \lambda_0) \beta \hbar^2 / m_e] k^2 + (\Delta - \xi \sigma \lambda_0)^2 \right\}^{1/2}, \quad (12)$$

which is the major result employed to describe the energy dispersion of MoS_2 in this paper. It should be noticed that the $\simeq k^4$ terms, trigonal warping and anisotropy are all considered as non-essential even though they may produce certain discrepancies in the calculated DOS.¹¹¹ We also find (see Appendix A) that the curvature of MoS_2 energy subbands is usually so small that even the highest possible doping density 10^{13} cm^{-2} only leads to $E_F \sim \lambda_0$. Thus, at zero or low T , we will not consider any high-energy corrections to Eq. (12). At very high T , on the other hand, the electronic states far from the Dirac point could be thermally populated by electrons.⁹¹ In this case, our model Hamiltonian in Eq. (11) and the simplified dispersion relation in Eq. (12) become inaccurate. Therefore, our main focus here will be limited to *small but finite* T for which the doping density and E_F can still play an important role in selecting convolution paths beyond the $\mathcal{O}(T^2/T_F^2)$ approximation introduced in Ref. [70].

Similar to buckled honeycomb lattices, the spin and valley indices of MoS_2 always appear as a product. Therefore, we can use a single composite index $\nu = \xi \sigma$ to specify an energy band for the rest of our discussion. By neglecting the mass terms in Eq. (12) as a vanishing-curvature approximation (formally $m_e \rightarrow \infty$),⁹³ the result in Eq. (12) reduces to

$$\varepsilon_{\gamma}^{\nu}(k) \simeq \nu \lambda_0 / 2 + \gamma \sqrt{(t_0 a_0)^2 k^2 + (\Delta - \nu \lambda_0)^2 / 4}. \quad (13)$$

This simplified expression has a few advantages, including simplicity and its formal resemblance to gapped graphene, so that known DOS, wave function, polarizability and many other quantities can be adopted. Additionally, it also provides an adequate description for the band structure of MoS_2 by taking into account a large gap parameter and ν -dependent splitting of two hole subbands. Nevertheless, we still find that the mass terms must be taken into account for accurate evaluations of the DOS and most other T -dependent electronic properties of MoS_2 . As demonstrated in Appendix A, even in the simplest parabolic approximation for $k \rightarrow 0$, the mass terms lead to a contribution comparable to the Dirac cone and bandgap parts of the Hamiltonian in Eq. (11). On the other hand, a very small curvature of energy subbands due to a large bandgap gives rise to a tremendous DOS (proportional to effective mass). Therefore, even a correction term $\alpha/(4m_e)$, which is hardly noticeable in the electron band structure, becomes significant for DOS. In fact, we have to drop the oversimplified result in Eq. (13) in calculations of the DOS, and the importance of the mass and higher-order terms for plasmon dispersion was discussed in Ref. [38].

Calculated energy dispersions and DOS of MoS_2 are presented in Fig. 3. For MoS_2 , we only consider the K valley $\xi = 1$ with a single bandgap Δ and a hole subband splitting $2\lambda_0$. The MoS_2 energy dispersions in (a) are very weak due to its very large bandgap Δ , and the k -dependent spin dependence of electron energy bands is also small. By taking into account all the terms in Eq. (11), a rigorous numerical calculation is performed and the exact DOS result of MoS_2 is presented in (b). As can be seen, whenever a subband is populated, a step occurs in the DOS. Since no electronic and hole states are available inside the gap region, we simply have $\rho_d(\mathbb{E}) = 0$ for $-(\Delta/2 - \lambda_0) < \mathbb{E} < \Delta/2$. Although the energy difference calculated from Eqs. (12) and (13) is small in (a) for electron and hole subbands, the corresponding change of DOS in (b) is significant due to very small curvature of subbands. In fact, we find the DOS

TABLE I: Piecewise density of states $\rho_d(\mathbb{E}) = A_i + B_i \mathbb{E}$ of monolayer molybdenum disulfide for each of three non-degenerate subbands, along with $\rho_d(\mathbb{E}) = 0$ within the gap region $-\Delta/2 + \lambda_0 < \mathbb{E} < \Delta/2$.

Range Index	Energy Range	γ	ν	$A_i[1/(t_0 a_0^2)]$	$B_i[1/(t_0 a_0^2)]$
$i = 1$	$\mathbb{E} < -\Delta/2 - \lambda_0$	-1	+1	0.0174	-0.169
$i = 2$	$ \mathbb{E} + \Delta/2 < \lambda_0$	-1	-1	0.043	-0.308
$i = 3$	$\mathbb{E} > \Delta/2$	+1		0.078	+0.179

from Eq. (13) is nearly twice as large as the exact one.^{38,92} In contrast, the DOS calculated from Eq. (12) appears as a very good approximation to the exact one, especially in the low-energy range.

Numerically, we consider a piecewise linear approximation to $\rho_d(\mathbb{E})$ of MoS₂ for each of three subbands, i.e., $\rho_d(\mathbb{E}) = A_i + B_i \mathbb{E}$ and $\rho_d(\mathbb{E}) = 0$ within the gap region $-\Delta/2 + \lambda_0 < \mathbb{E} < \Delta/2$. The expansion coefficients $\{A_i, B_i\}$ for three subbands are listed in Table I. We adopt these coefficient values for $\rho_d(\mathbb{E})$, which arise from the exact numerical calculations in order to achieve the highest possible precision and credibility for our finite- T derivations. However, our effective model, presented in Appendix A, also gives out DOS results which show good agreement with these numerical values and could be applied to decisive estimates of various collective calculations for MoS₂ in the next section.

Once the piecewise linear DOS is found, we can easily calculate E_F for a fixed n of doped electrons (e) or holes (h). The new ingredient here is that the full $\rho_d(\mathbb{E})$ is not proportional to energy \mathbb{E} (different from Eq. (13)) so that E_F^e for spin-degenerate electron subbands is determined from

$$n_e = \left(E_F^e - \frac{\Delta}{2} \right) \left[A_3 + \frac{B_3}{2} \left(\frac{\Delta}{2} + E_F^e \right) \right], \quad (14)$$

or equivalently,

$$E_F^e = \frac{1}{2B_3} \left[-2A_3 + \sqrt{(2A_3 + B_3\Delta)^2 + 8n_e B_3} \right]. \quad (15)$$

For hole doping, on the other hand, its Fermi energy E_F^h differs from the electron doping case, i.e.,

$$E_F^h = \frac{1}{B_1} \left\{ -A_1 + \sqrt{-2B_1 n_h + \left[A_1 - B_1 \left(\frac{\Delta}{2} - \lambda_0 \right) \right]^2} \right\}, \quad (16)$$

where only the lowest hole subband is populated due to nearly flat dispersions of hole subbands. The calculated E_F^e and E_F^h as functions of n_e and n_h are shown in insets (i1) and (i2) of Fig. 4. Here, both the linear and quadratic E_F^e terms in the doping density equations are present (see Eq. (14)), and most importantly, *there is no symmetry* between electron and hole states. Unlike graphene, the linear dependence here dominates for both electrons and holes due to large energy bandgap Δ . Each Fermi-energy curve starts from the corresponding bandedge $\Delta/2 = 8.13E_0$ for electrons and $-\Delta/2 + \lambda_0 = -7.45E_0$ for holes. The well-known result for gapped graphene, i.e., $E_F^2 - \Delta_0^2 = \pi n (\hbar v_F)^2$ from Eq. (8), can be formally recovered from Eqs. (14) and (16) by setting $\lambda_0 = 0$, $A_{1,3} = 0$ and $|B_{1,3}| = 2/(\pi \hbar^2 v_F^2)$.

Based on our piecewise DOS model for MoS₂, $\mu(T)$ can be computed in a similar way, as we have done for buckled honeycomb lattices, except that we now need to evaluate *four* different terms related to two split hole subbands (see Eq. (B13)). The numerically calculated $\mu(T)$ of MoS₂ are presented in Fig. 4. As discussed above, the most special property of MoS₂ is the broken electron/hole symmetry. Consequently, $\mu(T)$ for electron doping switches from positive to negative at $k_B T \approx 2.5 E_0$, while $\mu(T)$ for hole doping remains negative. Broken electron-hole symmetry leads to two substantially different ways to select various paths for a thermal convolution. In comparison with other Dirac materials, MoS₂ can be considered as a unique material with different electron-hole symmetry properties and corresponding T dependence in $\mu(T)$.

III. TEMPERATURE-DEPENDENT PLASMON MODES

After the discussion in Sec. II on selecting different convolution paths based on field-tunable bandgaps and gate-depleted electron doping densities, we now turn to thermal convolutions for temperature-dependent dielectric prop-

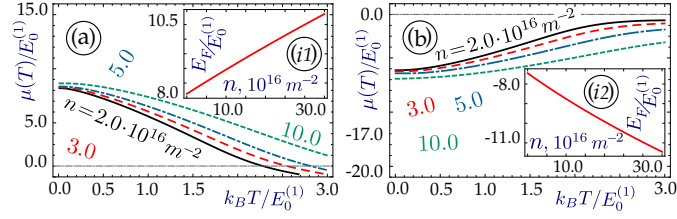


FIG. 4: (Color online) Calculated $\mu(T)$ for MoS_2 . Panels (a) and (b) present $\mu(T)$ as functions of T for various electron [in (a)] and hole [in (b)] doping densities: $n = 2.0 \times 10^{12} \text{ cm}^{-2}$ (black solid curve), $3.0 \times 10^{12} \text{ cm}^{-2}$ (red dashed curve), $5.0 \times 10^{12} \text{ cm}^{-2}$ (blue dash-dotted curve) and $10.0 \times 10^{12} \text{ cm}^{-2}$ (green short-dashed curve). Insets (i1) and (i2) illustrate how E_F depends on n at $T = 0$.

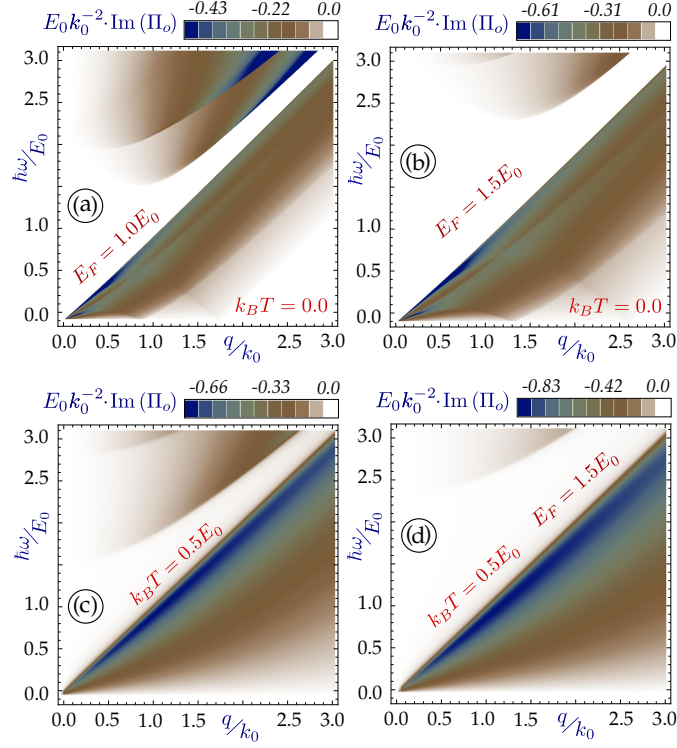


FIG. 5: (Color online) Single-particle excitation regions or particle-hole modes, outlined by non-zero $\text{Im}[\Pi_T(q, \omega | \mu, T)]$ at an arbitrary T for silicene with $\Delta_{SO}/E_0 = 0.7$ and $\Delta_z/E_0 = 0.2$. The upper panels (a) and (b) are for $T = 0$, while the lower plots (c) and (d) are for $k_B T/E_0 = 0.5$. Moreover, left panels (a) and (c) correspond to $E_F/E_0 = 1.0$, whereas the right ones correspond to $E_F/E_0 = 1.5$. The white regions for $\text{Im}[\Pi_T(q, \omega | \mu, T)] = 0$ specify damping-free plasmon-excitation regions.

erties in silicene and molybdenum disulfide 2D materials. As one of the most relevant applications of our analytically calculated $\mu(T)$, we consider plasmon modes in a doped and self-sustained gapped Dirac cone material. The plasmon dispersion relation can be obtained from zeros of the system dielectric function $\epsilon_T(q, \omega)$, which is calculated within the random-phase approximation (RPA) as

$$\epsilon_T(q, \omega) = 1 - v(q) \Pi_T(q, \omega | \mu, T) = 0, \quad (17)$$

where $v(q) = e^2/2\epsilon_0\epsilon_r q$ is the Fourier-transformed 2D Coulomb potential, and ϵ_r is the dielectric constant of the 2D material. At finite T , the dynamical polarization function $\Pi_T(q, \omega | \mu, T)$ in Eq. (17) for electron doping can be acquired from a thermal convolution⁸⁴ of its $T = 0$ counterpart $\Pi_0(q, \omega | E_F)$, i.e.,

$$\Pi_T(q, \omega | \mu, T) = \frac{1}{2k_B T} \int_0^\infty d\xi \frac{\Pi_0(q, \omega | \xi)}{1 + \cosh[(\mu - \xi)/k_B T]}, \quad (18)$$

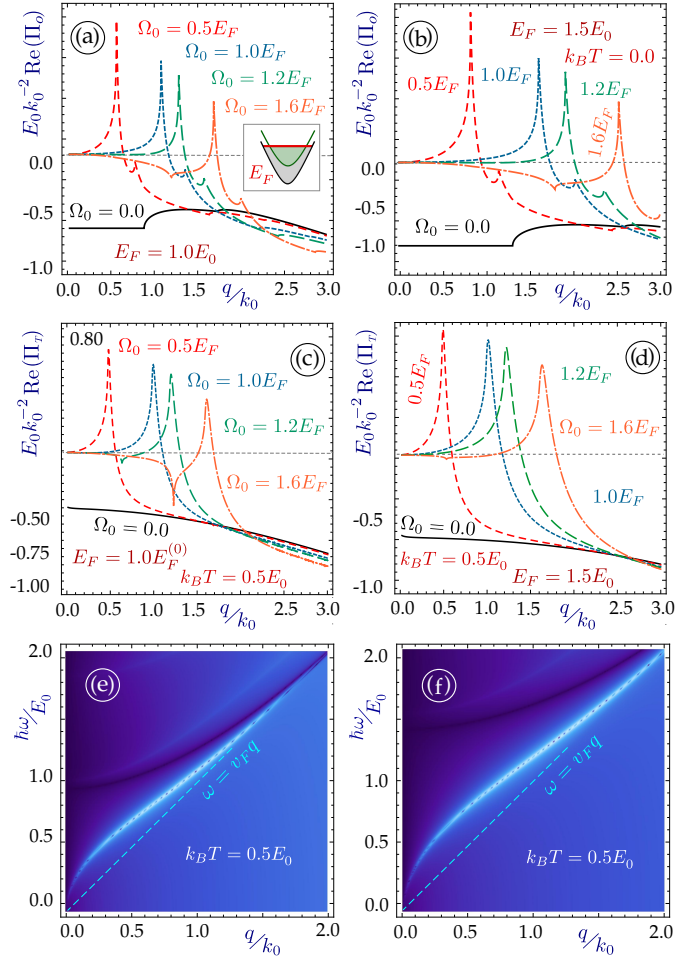


FIG. 6: (Color online) Dynamic polarization functions and plasmon dispersions for silicene with $\Delta_{SO}/E_0 = 0.7$ and $\Delta_z/E_0 = 0.2$, where both subbands are populated at $T = 0$. Panels (a)-(d) present $\text{Re}[\Pi_T(q, \omega | \mu, T)]$ at $\omega = \Omega_0$ as a function of q , where $\hbar\Omega_0/E_0 = 0.0, 0.5, 1.0, 1.2$ and 1.6 are indicated by black solid, red dashed, blue short-dashed, green long-dashed and orange dash-dotted curves, respectively. Panels (a)-(b) are for $T = 0$, while (c)-(d) for $k_B T/E_0 = 0.5$. Moreover, we set $E_F/E_0 = 1.0$ in (a) and (c) while $E_F/E_0 = 1.5$ for (b) and (d). Plasmon dispersions at $k_B T/E_0 = 0.5$ are presented in plot (e) for $E_F/E_0 = 1.0$ and in (f) for $E_F/E_0 = 1.5$.

where electron doping is assumed. The chemical potential μ as functions of both temperature T and the Fermi energy E_F characterizes a specific selection of a convolution path for a particular material band structure, and $(1/2k_B T)\{1 + \cosh[(\mu - \xi)/k_B T]\}^{-1}$ can be regarded as the response function for a preselected thermal convolution of fermions. The thermal convolution of the $T = 0$ polarizability in Eq. (18) is quite similar for buckled honeycomb lattices and MoS₂, since in both cases their low-energy band structure is characterized by two inequivalent doubly-degenerate pairs of subbands labeled by a composite index $\nu = \sigma \xi$. For a doubly-degenerate pair, its zero- T polarization function $\Pi_0^{(\nu)}$ in the one-loop approximation takes the form

$$\Pi_0^{(\nu)}(q, \omega | E_F) = \frac{1}{4\pi^2} \int d^2 \mathbf{k} \sum_{\gamma, \gamma' = \pm 1} \left[1 + \gamma \gamma' \frac{\mathbf{k} \cdot (\mathbf{k} + \mathbf{q}) + \Delta_\nu^2}{|\varepsilon_\gamma^\nu(k) \varepsilon_{\gamma'}^\nu(|\mathbf{k} + \mathbf{q}|)} \right] \frac{\Theta(E_F - \varepsilon_\gamma^\nu(k)) - \Theta(E_F - \varepsilon_{\gamma'}^\nu(|\mathbf{k} + \mathbf{q}|))}{\hbar(\omega + i0^+) + \varepsilon_\gamma^\nu(k) - \varepsilon_{\gamma'}^\nu(|\mathbf{k} + \mathbf{q}|)}, \quad (19)$$

where $\gamma = \pm 1$ labels the electron and hole states, while $\nu \equiv \sigma \xi = \pm 1$ corresponds to two combinations of spin and valley gaps. Moreover, the zero- T dynamical polarization function introduced in Eq. (18) is obtained from

$$\Pi_0(q, \omega | E_F) = \sum_{\nu = \pm 1} \Pi_0^{(\nu)}(q, \omega | E_F). \quad (20)$$

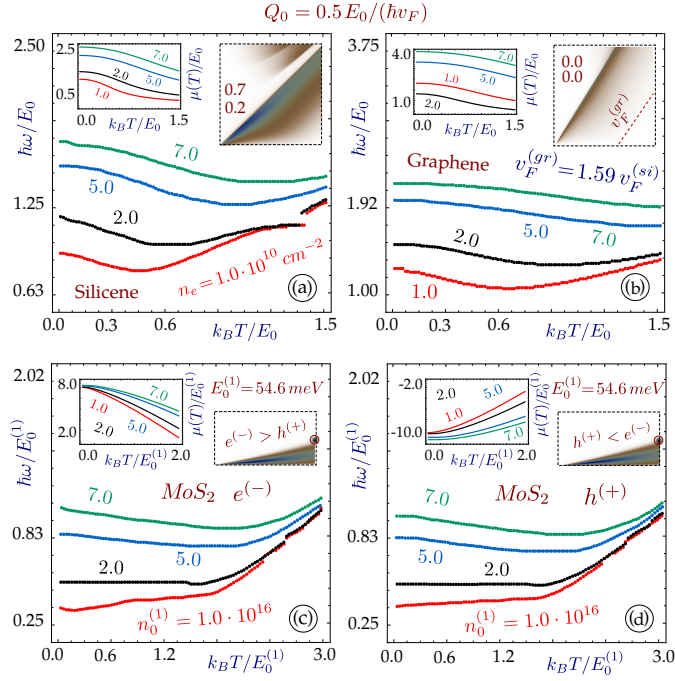


FIG. 7: (Color online) Plasmon modes, obtained from the solutions of $\text{Re}[\epsilon(Q_0, \omega | \mu, T)] = 0$, for silicene, graphene and molybdenum disulfide with various electron densities n_0 as a function of T . Panel (a) presents the plasmon frequencies for silicene with $\Delta_{SO}/E_0 = 0.7$ and $\Delta_z/E_0 = 0.2$. Panel (b) is for gapless graphene with $v_F = 8.6 \times 10^7$ m/s. In both (a) and (b), each curve corresponds to: $n_0 = 1.0 \times 10^{10}$ cm^{-2} (red), 2.0×10^{10} cm^{-2} (black), 5.0×10^{10} cm^{-2} (blue) and 7.0×10^{10} cm^{-2} (green). Plots (c) and (d) show T -dependent plasmons for electron- and hole-doped MoS₂ in the unit of $E_0^{(1)} = 54.6$ meV. Here, various curves are attributed to: $n_0 = 1.0 \times 10^{12}$ cm^{-2} (red), 2.0×10^{12} cm^{-2} (black), 5.0×10^{12} cm^{-2} (blue) and 7.0×10^{12} cm^{-2} (green). A fixed wave vector $Q_0 = E_0/(\hbar v_F)$ is set for each plot, where $v_F^{(gr)} = 1.59 v_F^{(si)}$ and $v_F^{(mo)} = a_0 t_0 = 0.47 \hbar v_F^{(gr)}$. There are two insets within each panel, showing the T -dependent chemical potential for each case and electron-hole modes at $T = 0$.

Numerical results of Eq. (18) at finite T are presented in Figs. 5 and 6 for dynamical polarization functions and additionally for plasmon dispersions in Figs. 6 and 7.

We first discuss the imaginary part of the polarizability $\text{Im}[\Pi_T(q, \omega | \mu, T)]$ since it specifies the regions and intensity of plasmon damping. It is found that the plasmon dissipation usually increases with T and the regions for damping-free plasmon excitation shrink dramatically at the same time, as shown in Fig. 5. Once T becomes high enough, however, $\text{Im}[\Pi_T(q, \omega | \mu, T)]$ shows a reduction scaled as $1/T$.^{70,91} Therefore, the T dependence of plasmon dissipation is not uniform on a fixed convolution path $\mu(T)$. Doping density, on the other hand, broadens the plasmon-excitation regions, as demonstrated by Fig. 5. As a result, the thermal and doping effects are expected to compete with each other in controlling plasmon dissipations by selecting different convolution paths with various doping densities or Fermi energies.

The plasmon dispersions at finite T are compared in Figs. 6(e) and 6(f) for two values of E_F or doping densities, where the plasmon energy is slightly pushed up by increased doping at this elevated T . We have also presented $\text{Re}[\Pi_T(q, \omega | \mu, T)]$ in Figs. 6(a)-6(d), where the peaks in $\text{Re}[\Pi_T(q, \omega | \mu, T)]$ must be kept positive in order to find a real solution of Eq. (17) for a plasmon mode. Obviously, increased E_F always pushes $\text{Re}[\Pi_T(q, \omega | \mu, T)]$ peaks to higher q values at a low T for fixed ω , implying a smaller group velocity and lower energy of the plasmon mode. On the other hand, the rise of T shifts $\text{Re}[\Pi_T(q, \omega | \mu, T)]$ peaks to lower q values for a higher doping.

In all our numerical calculations, we used $\hbar\gamma = 0.01 E_0 = 6.28 \times 10^{-5}$ eV. The effect of such broadening on the width of the plasmon branch is found negligible, especially at finite temperatures for which the imaginary part of the dynamical polarization function is nonzero at nearly all frequencies and wave vectors, as displayed in Figs. 5 (c) and (d).

Graphene and silicene, shown in Fig. 7 (a) and (b), differ by the Fermi velocities as well as the existence of the energy gap. In our calculation with a fixed electron density for each curve, the major difference is found from the Fermi velocity due to the $1/v_F^2$ dependence in Eq. (9). We used larger electron densities $\sim 10^{16}$ m^{-2} for MoS₂ in order to make the Fermi energy at least slightly distinguishable from the bandedges. The corresponding energy unit

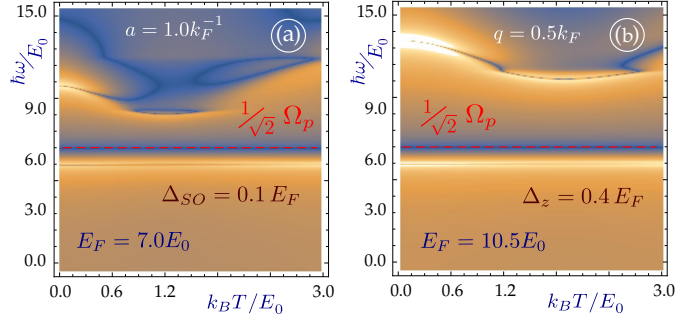


FIG. 8: (Color online) T -dependent nonlocal plasmon modes for a silicene-based hybrid system with $\Delta_{SO}/E_F = 0.1$ and $\Delta_z/E_F = 0.4$. Density plots of the real part of $\mathbb{S}_c(q, \omega|\mu, T)$ for fixed $q/k_F = 0.3$ are presented. Here, panel (a) corresponds to an intrinsic system with $E_F/E_0 = 7.0$, while plot (b) is for $E_F/E_0 = 10.5$.

is $E_0^{(1)} = 54.6 \text{ meV}$ which was decided in a similar way with the Fermi velocity $a_0 t_0 = 0.47 v_F^{(gr)}$. For such electron doping, the plasmon dispersion in the long-wavelength limit $\Omega_p^2 \sim q (t_0 a_0 / \Delta_0)^2 E_F n$, where the Fermi energy E_F has the same order of magnitude and little above the bandgap Δ_0 in the conduction band.

From Fig. 7 we find that similar temperature dependence is seen for all the cases with various doping values and temperature ranges, i.e., the branch is lowered first, reaching a minimum, then monotonically increases for intermediate and finite temperatures. Particularly, we find in molybdenum disulfide that the plasmon branches for electron doping are slightly higher than those for hole doping, which is in agreement with the zero-temperature results in Ref. [38]. However, the electron/hole asymmetry is relatively small for intermediate temperatures $k_B T \simeq 2.0 E_0^{(1)}$.

The selection of a convolution path can not only affect plasmon modes at finite T , but also influence their interaction with the surrounding environment in so-called 2D open systems (2DMOS). Let us consider a typical hybrid nanostructure in graphene-based devices, ^{94,95} which consists of a 2D layer (2DEG, graphene, buckled honeycomb layer, or MoS₂) coupling with surface plasmons supported by a semi-infinite conductor. ^{96,97} Although plasmon excitations in a closed system are solely determined by two-particle Green's functions, they become more complicated in 2DMOS, depending on the Coulomb interaction with the environment. ^{98,99} The key player in this 2DMOS is the screened Coulomb coupling between electrons in 2D materials and within a conducting substrate. ⁴² Such a screened potential could be found from a nonlocal frequency-dependent inverse dielectric function. ¹⁰⁰⁻¹⁰³ Consequently, two ⁹⁷ or more ¹⁰⁴ acoustic-like plasmon branches were predicted and verified experimentally. ^{64,105} At finite T , plasmon coupling to an external electron reservoir is highlighted by occurrence of additional plasmon-dissipation channels. ⁹¹

The plasmon branches in 2DMOS are obtained from zeros of the so-called structure factor $\mathbb{S}_c(q, \omega|\mu, T)$, playing the role of a dielectric function $\epsilon_T(q, \omega)$ in Eq. (17) for a self-sustained layer. Here, the structure factor is calculated as ^{91,97}

$$\mathbb{S}_c(q, \omega|\mu, T) = 1 - v(q) \Pi_T(q, \omega|\mu, T) \left[1 + \frac{1 - \epsilon_B(\omega)}{1 + \epsilon_B(\omega)} e^{-2qa} \right], \quad (21)$$

where a is the distance between the 2D layer and the conductor surface, the conductor dielectric function in the local limit is given by $\epsilon_B(\omega) = 1 - \Omega_p^2/\omega^2$, Ω_p is the bulk-plasma frequency defined by $\Omega_p^2 = (N_m e^2)/(4\pi\epsilon_0\epsilon_b M^*)$, N_m is the electron concentration, M^* is the effective mass of electrons, and ϵ_b is the substrate dielectric constant. This local approximation stays valid for a large range of wave vectors $q \ll 2 \times 10^7 \text{ cm}^{-1}$ since the Fermi wavelength in metals becomes comparable with the inverse lattice constant. As a result, the frequency of the calculated upper plasmon branch in Fig. 8, which equals $\Omega_p/\sqrt{2}$ as $q \rightarrow 0$, might range from ultra-violet (metal substrate) down to infrared or even terahertz (doped semiconductor substrate).

Previously, we reported that for spin- and valley-dependent single-particle excitations in a 2D layer ⁹² (which is also true for buckled honeycomb lattices and MoS₂), such a hybrid structure could be used to measure surrounding dielectric properties or spin-orbit couplings because the energy and damping rate of each plasmon branch are determined independently by band-structure parameters of the 2D layer. As an example, two plasmon branches in silicene or MoS₂ depend on bandgaps as $\Delta_i^{1/2}$ or $\Delta_i^{1/4}$ ($i = >$ or $<$), but the outermost single-particle excitation boundaries are determined solely by $\Delta_<$. Therefore, it is believed that an additional linear plasmon branch in this hybrid system can provide us with new information on surrounding materials.

In the present work, we add effects of finite doping and temperature into silicene-based hybrid systems. Our numerical results for nonlocal plasmon modes are presented in Fig. 8. Here, we find both dispersion and damping of the two plasmon branches are substantially modified with respect to $E_F = 7.0 E_0$ and $E_F = 10.5 E_0$ by selecting two different thermal-convolution paths. At the considered temperature range, the plasmon modes are mostly damped. Here, the upper branch always stays above the surface plasmon $\Omega_p/\sqrt{2}$. These modes become nearly undamped for higher temperatures.

IV. CONCLUDING REMARKS

In this paper, we have carried out an extensive investigation of gapped Dirac materials with doping at finite T and obtained a set of explicit equations determining $\mu(T)$ for the system. The system we considered include graphene, with or without an energy gap, buckled honeycomb lattices with spin- and valley-dependent energy subbands and reduced degeneracy, as well as the transition metal dichalcogenides having broken symmetry between electron and hole states. Our results could also be employed to calculate $\mu(T)$ at finite T for parabolic or quasi-parabolic energy subbands in semiconductors with doped light or heavy holes.^{106,107} In general, our model is limited only by the linear dependence in the DOS which remains valid over a wide energy range for all materials mentioned above.

Physically, we have demonstrated that $\mu(T)$ depends substantially on the energy bandgap(s) of the materials considered here since the DOS depends on the curvature of each subband. Specifically, we studied structures with two non-degenerate, spin- and valley-resolved energy subbands for both valence and conduction electrons, such as silicene. The upper subband could still receive a thermal population even if it is an undoped sample. Such a phenomenon is always seen as an enhanced reduction rate in $\mu(T)$ whenever the initially-empty upper subband becomes thermally occupied. Consequently, one can always tune the T -dependence in $\mu(T)$ by bringing E_F very close to the bottom of an empty upper subband. Similar behavior also occurs in quantum wells and quasi-one-dimensional nanoribbons,¹⁰⁸ which could be treated equally by our model.

In addition, we would like to emphasize that the T dependence in $\mu(T)$ relies on a symmetry between electron and hole states. If such a DOS symmetry can be maintained for electrons and holes around a Dirac point, e.g., silicene, $\mu(T)$ will keep its sign unchanged. For MoS₂, on the other hand, $\mu(T)$ is able to change its sign since no symmetry between electron and hole states exists. In calculating the DOS of MoS₂, we have developed a piecewise-linear model assisted by the Hamiltonian parameters, which provides exact results for $\rho_d(\mathbb{E})$ at the bandedges, and becomes a good approximation for the DOS at very high energies.

Furthermore, besides tuning by doping density, we have demonstrated that the band structures of silicene and MoS₂ can also be tuned effectively by applying a perpendicular electric field, which facilitates varying the T dependence in $\mu(T)$. As a result, a pre-selected path can be input into a response function for thermal convolutions, acquiring a unique thermal dependence in collective electronic properties. Quantitatively, we have found that doping can affect plasmon dispersions, given by $(\hbar\omega/E_F)^2 \simeq \Lambda q$ in which Λ is regarded as an effective length depending on E_F . On the other hand, in the absence of doping, the thermal excitations of electrons at finite T can still produce a nonzero polarization function⁷⁰, giving rise to a plasmon dispersion proportional to $(qT)^{1/2}$.

Technically, the selection of a particular path for thermal convolutions can be adopted for engineering the T dependence of plasmon dispersions and damping. The thermal shift of plasmon frequency is expected to be used for remotely measuring the local dielectric environment and local hot-electron temperature in nano-plasmonic structures and transistors, respectively.

Acknowledgments

D.H. would like to thank the support from the Air Force Office of Scientific Research (AFOSR).

Appendix A: Density-of-states

Silicene and Germanene

The DOS of electron and hole states with energy dispersion $\varepsilon_{\vec{\gamma},\sigma}^{\xi}(k)$ is defined as

$$\rho_d(\mathbb{E}) = \int \frac{d^2\mathbf{k}}{(2\pi)^2} \sum_{\gamma=\pm 1} \sum_{\xi, \sigma=\pm 1} \delta(\mathbb{E} - \varepsilon_{\gamma}^{\xi, \sigma}(k)) , \quad (\text{A1})$$

where $\xi = \pm 1$ and $\sigma = \pm 1$ are valley and spin indices which always appear as a product $\sigma\xi$. We use a single composite index $\nu = \sigma\xi = \pm 1$ to specify doubly-degenerated energy bands and the transformation $\sum_{\xi, \sigma=\pm 1} \implies 2 \sum_{\nu=\pm 1}$ for summations over band indices.

In calculating the DOS in Eq. (A1), the following identity has been employed, i.e.,

$$\delta(f(x)) = \sum_i \frac{\delta(x - x_i)}{\left| \frac{df(x)}{dx} \right|_{x=x_i}} , \quad (\text{A2})$$

where x_i are the roots of $f(x) = 0$. By using Eqs. (A1) and (A2), the DOS calculation for both silicene and germanene can be done in a straightforward way, yielding

$$\rho_d(\mathbb{E}) = \frac{1}{\pi} \sum_{\gamma=\pm 1} \frac{\gamma \mathbb{E}}{\hbar^2 v_F^2} \sum_{i=<, >} \Theta\left(\frac{\mathbb{E}}{\gamma} - \Delta_i\right) , \quad (\text{A3})$$

which indicates that the DOS for gapped Dirac systems is still linear in \mathbb{E} similar to graphene. However, it is nonzero only outside the gap region $|\mathbb{E}| > \Delta_{<}$. The result in Eq. (A3) also applies to gapped graphene, where $\Delta_{<} = \Delta_{>} = \Delta_0$. Moreover, the well-known V-shaped $\rho_d(\mathbb{E})$ for gapless graphene can also be reproduced after taking $\Delta_{<, >} \rightarrow 0$.

Molybdenum Disulfide

Here, we look into three effective models with different complexities and accuracies for MoS₂ energy dispersion. First, we use the simplified energy dispersion in Eq. (13), in which we leave out two mass terms proportional to α and β . As shown in Fig. 3(a), Eq. (13) yields pretty accurate results for energy eigenstates. In a similar way, after inserting Eq. (13) into Eqs. (A1) and (A2), we find

$$\rho_d(\mathbb{E}) = \frac{1}{\pi (t_0 a_0)^2} \sum_{\gamma=\pm 1} \frac{1}{\gamma} \sum_{\nu=\pm 1} \left(\mathbb{E} - \frac{\nu}{2} \lambda_0 \right) \Theta\left(\gamma \left(\mathbb{E} - \frac{\nu \lambda_0}{2} \right) - \frac{1}{2} (\Delta - \nu \lambda_0) \right) , \quad (\text{A4})$$

However, the result in Eq. (A4) does not match the numerical one, as seen from Fig. 3(b). By including the mass terms under the parabolic-subband approximation, we obtain the following energy dispersion

$$\varepsilon_{\gamma}^{\nu}(k) = \frac{1}{2} [\nu \lambda_0 (1 - \gamma) + \gamma \Delta] + \left[\frac{\hbar^2}{4m_e} (\alpha + \gamma\beta) + \frac{\gamma (t_0 a_0)^2}{\Delta - \nu \lambda_0} \right] k^2 . \quad (\text{A5})$$

Equation (A5) leads to the DOS, given by⁹²

$$\rho_d(\mathbb{E}) = \frac{1}{2\pi \hbar^2} \sum_{\gamma, \nu=\pm 1} \left| \frac{\alpha + \gamma\beta}{4m_e} + \frac{\gamma (t_0 a_0)^2}{\hbar^2 (\Delta - \nu \lambda_0)} \right|^{-1} \Theta\left(\gamma \left(\mathbb{E} - \frac{\nu \lambda_0}{2} \right) - \frac{1}{2} (\Delta - \nu \lambda_0) \right) . \quad (\text{A6})$$

Equation (A6) includes both the α and β mass terms due to vanishing curvature of each subband at $k = 0$ by a large bandgap Δ . The importance that the mass and even higher-order terms must be taken into account for calculating plasmon modes was discussed in Ref. [38].

Going beyond the parabolic-subband approximation, we keep all the terms except for the nonessential ones $\mathcal{O}(k^4)$ in energy dispersion, leading to

$$\varepsilon_\gamma^\nu(k) \simeq \frac{1}{2} \nu \lambda_0 + \frac{\hbar^2 \alpha}{4m_e} k^2 + \frac{\gamma}{2} \sqrt{(\Delta - \nu \lambda_0)^2 + \left[(2t_0 a_0)^2 + (\Delta - \nu \lambda_0) \frac{\hbar^2 \beta}{m_e} \right] k^2} . \quad (\text{A7})$$

Here, we employ a general equation from our previous work⁹² to construct a linear approximation which is valid for all experimentally accessible electron and hole doping densities.^{38,92} By substituting Eq. (A7) into Eq. (A1), we get

$$\rho_d(\mathbb{E}) = \frac{1}{2\pi} \sum_j \sum_{\gamma, \nu=\pm 1} \left| \tilde{\alpha} + \frac{\gamma \tilde{A}_\nu(\Delta \pm \lambda_0, \beta | a_0 t_0)}{2 \left\{ \mathbb{E} - \tilde{\varepsilon}_\nu - \tilde{\alpha} \xi_\nu^{(j)}(\mathbb{E}) \right\}} \right|^{-1} \Theta \left(\gamma \left(\mathbb{E} - \frac{\mu \lambda_0}{2} \right) - \frac{1}{2} (\Delta - \nu \lambda_0) \right) , \quad (\text{A8})$$

where $\tilde{\varepsilon}_\nu = \nu \lambda_0 / 2$, $\tilde{\Delta}_\nu = (\Delta - \nu \lambda_0) / 2$, $\tilde{A}_\nu(\Delta \pm \lambda_0, \beta | a_0 t_0) = (\Delta - \nu \lambda_0) \hbar^2 \beta / 4m_e + (t_0 a_0)^2$, and $\tilde{\alpha} = \hbar^2 \alpha / 4m_e$. In addition, $\xi_\nu^{(j)}(\mathbb{E})$ represents the j th root of equation $\mathbb{E} - \tilde{\varepsilon}_\nu - \alpha \xi - \gamma \sqrt{\tilde{A}_\nu \xi + \tilde{\Delta}_\nu^2} = 0$. This root equation can be rewritten as $(\alpha \xi)^2 + B \xi + C = 0$, where $B = \tilde{A}_\nu + 2\alpha$ and $C = (\mathbb{E} - \tilde{\varepsilon}_\nu)^2 - \tilde{\Delta}_\nu^2$. The only physical solution for this root equation is $\xi_\nu^{(1)}(\mathbb{E}) = 1/(2\alpha)^2 (B + \sqrt{B^2 - 4\alpha^2 C})$ (another spurious solution has been discarded), which is independent of $\gamma = \pm 1$. Explicitly, this root $\xi_\nu^{(1)}(\mathbb{E})$ can be written as

$$\xi_\nu^{(1)}(\mathbb{E}) = \frac{1}{2\tilde{\alpha}^2} \left\{ \tilde{A}_\nu + 2\tilde{\alpha} \left(\mathbb{E} - \tilde{\varepsilon}_\nu^{(0)} \right) - \left[\tilde{A}_\nu^2 + 4\tilde{\alpha}^2 \tilde{\Delta}_\nu^2 + 4\tilde{\alpha} \tilde{A}_\nu \left(\mathbb{E} - \tilde{\varepsilon}_\nu^{(0)} \right) \right]^{1/2} \right\} , \quad (\text{A9})$$

which is accurate in the sense that no other approximations have been taken except for the nonessential ones $\mathcal{O}(k^4)$ in energy dispersion Eq. (A7). Substituting Eq. (A9) into Eq. (A8) gives the DOS at an arbitrary energy \mathbb{E} for both electrons and holes.

For simplicity, however, we only consider the DOS next to each subband edge. In this case, we write $\varepsilon_1^\nu(k) = \Delta/2 + \delta\epsilon$ for $\delta\epsilon \ll \mathbb{E} \approx \Delta/2$, which leads to

$$\xi_\nu^{(1)} \simeq \frac{4m_e}{\alpha \hbar^2} \left\{ 1 - \frac{(a_0 t_0)^2 + \hbar^2 \beta / (4m_e) (\Delta - \nu \lambda_0)}{(a_0 t_0)^2 + \hbar^2 / (4m_e) [(\alpha + \beta) (\Delta - \nu \lambda_0)]} \right\} \delta\epsilon , \quad (\text{A10})$$

and the DOS is approximated as

$$\rho_d(\mathbb{E}) = \frac{1}{2\pi} \sum_{\nu=\pm 1} \left[\frac{\Delta - \nu \lambda_0}{(a_0 t_0)^2 + \hbar^2 / (4m_e) (\alpha + \beta) (\Delta - \nu \lambda_0)} + \frac{2\delta\epsilon [(a_0 t_0)^2 + \hbar^2 \beta / (4m_e) (\Delta - \nu \lambda_0)]^2}{\{(a_0 t_0)^2 + \hbar^2 / (4m_e) [(\alpha + \beta) (\Delta - \nu \lambda_0)]\}^3} \right] . \quad (\text{A11})$$

Numerically, we rewrite the above equation with two parameters $c_0^{(3)}$ and $c_1^{(3)}$ as

$$\begin{aligned} \rho_d(\mathbb{E}) &= c_0^{(3)} + c_1^{(3)} \left(\mathbb{E} - \frac{\Delta}{2} \right) , \\ c_0^{(3)} &= 0.180 \frac{1}{t_0 a_0^2} = 11.74 \frac{E_0}{(\hbar v_F)^2} , \\ c_1^{(3)} &= 0.268 \frac{1}{(t_0 a_0)^2} = 1.218 \frac{1}{(\hbar v_F)^2} , \end{aligned} \quad (\text{A12})$$

where $E_0 = 5.22 \text{ meV}$ is the scale of energy used in numerical calculations. For two valence subbands, their DOS can be parameterized in a similar way. For $\gamma = -1$, $\nu = 1$ and $\mathbb{E} \approx -\Delta/2 + \lambda_0$, we find $\rho_d(\mathbb{E}) = c_0^{(2)} + c_1^{(2)} \left[\mathbb{E} - \left(\frac{\Delta}{2} - \lambda_0 \right) \right]$ with the two expansion coefficients given by

$$\begin{aligned} c_0^{(2)} &= \frac{1}{2\pi} \frac{\Delta - \lambda_0}{(a_0 t_0)^2 + (\beta - \alpha) (\Delta - \lambda_0)} , \\ c_1^{(2)} &= \frac{1}{\pi} \frac{\delta\epsilon [(a_0 t_0)^2 + \hbar^2 \beta / (4m_e) (\Delta - \lambda_0)]^2}{\{(a_0 t_0)^2 + \hbar^2 / (4m_e) [(\beta - \alpha) (\Delta - \lambda_0)]\}^3} < 0 , \end{aligned} \quad (\text{A13})$$

or numerically,

$$\begin{aligned} c_0^{(2)} &= 0.105 \frac{1}{t_0 a_0^2} = 6.847 \frac{E_0}{(\hbar v_F)^2} , \\ c_1^{(2)} &= -0.232 \frac{1}{(t_0 a_0)^2} = -1.051 \frac{1}{(\hbar v_F)^2} . \end{aligned} \quad (\text{A14})$$

Finally, for the lower hole subband with $\mathbb{E} \approx -\Delta/2 - \lambda_0$, we obtain

$$\begin{aligned} \rho_d(\mathbb{E}) &= c_0^{(2)} + c_1^{(2)} \left[\mathbb{E} - \left(\frac{\Delta}{2} + \lambda_0 \right) \right] , \\ c_0^{(1)} &= \frac{1}{2\pi} \sum_{\nu=\pm 1} \frac{\Delta - \nu \lambda_0}{(a_0 t_0)^2 + (\beta - \alpha)(\Delta - \nu \lambda_0)} , \\ c_1^{(1)} &= \frac{1}{\pi} \sum_{\nu=\pm 1} \frac{\delta\epsilon \left[(a_0 t_0)^2 + \hbar^2 \beta / (4m_e) (\Delta - \nu \lambda_0) \right]^2}{\left\{ (a_0 t_0)^2 + \hbar^2 / (4m_e) [(\beta - \alpha) (\Delta - \nu \lambda_0)] \right\}^3} < 0 , \end{aligned} \quad (\text{A15})$$

or numerically,

$$\begin{aligned} c_0^{(1)} &= 0.233 \frac{1}{t_0 a_0^2} = 15.17 \frac{E_0}{(\hbar v_F)^2} , \\ c_1^{(1)} &= -0.458 \frac{1}{(t_0 a_0)^2} = 2.077 \frac{1}{(\hbar v_F)^2} . \end{aligned} \quad (\text{A16})$$

It is straightforward to obtain our previous DOS results for the gapped graphene model (A4) after setting $\alpha = \beta = 0$. We also note that the slope of the DOS in the valence band is negative, as it should be according to Fig. 1(b), and the summation over the ν index is present in all cases (with $\xi = 1$) except for the upper hole subband in Eqs. (A13).

Our results in Eqs. (A12)-(A16) (i.e., moving from conduction to valence bands or from right to left) represent a fairly good match with the previously obtained numerical values, specified in Sec. II and later used for all our finite T calculations. The coefficients $c_0^{(i)}$, $i = 1, 2, 3$ are equal to the giant discontinuities $\delta\rho_d(\mathbb{E})$ in the DOS at each subband edge, except for $c_0^{(1)} \simeq \delta\rho_d^{(2)}(-\Delta/2 + \lambda_0) + \delta\rho_d^{(1)}(-\Delta/2 - \lambda_0)$, and they are accurate. The linear coefficients $c_1^{(i)}$ are 20 – 25% larger, compared with the numerical results, since all the $\sim k^4$ terms in energy dispersions have been neglected. The inclusion of these terms leads to increased energies for a chosen wave vector and a decrease of the DOS. This discrepancy becomes larger for higher energies, which is seen well for $c_1^{(1)}$ with $\mathbb{E} < -\Delta/2 - \lambda_0$. However, such higher-energy states are kept undoped unless T is really high. For situations considered in this paper, we are limited to $\delta\epsilon \approx \lambda_0$ within two subband edges for holes. Within such a small energy range, we have $\delta\epsilon c_1^{(i)} \ll c_0^{(i)}$ so that the actual DOS values remain unaffected and our model yields accurate results.

Appendix B: Chemical potential at a finite temperature

$\mu(T)$ for Molybdenum Disulfide

In contrast to the previously discussed buckled honeycomb lattices and graphene, the electron/hole symmetry in MoS₂ becomes broken. Even with the simplest gapped graphene model given by Eq. (13), the two hole subbands are no longer degenerate, but are separated by λ_0 at $k = 0$. For the highest accessible doping densities $n < 10^{13} \text{ cm}^{-2}$, the lower hole subband could not be populated at $T = 0$. This can be verified by evaluating Eq. (B15) as

$$n_c = \frac{2}{\pi} \frac{\lambda_0 \Delta}{(t_0 a_0)^2} = 1.0 \times 10^{14} \text{ cm}^{-2} . \quad (\text{B1})$$

From now on, we will use a piecewise-linear model given by Eqs. (A12) - (A16) for the DOS with the empirical coefficients given in Appendix A. Let us first consider electron doping with density n_e . For this case, the corresponding Fermi energy E_F^e is determined by

$$n_e = \frac{c_1^{(3)}}{2} \left(E_F^2 - \frac{\Delta^2}{4} \right) + c_0^{(3)} \left(E_F - \frac{\Delta}{2} \right), \quad (\text{B2})$$

or

$$E_F^e = \frac{1}{c_1^{(3)}} \left\{ -c_0^{(3)} + \left[\left(c_0^{(3)} + c_1^{(3)} \frac{\Delta}{2} \right)^2 + 2n_e c_1^{(3)} \right]^{1/2} \right\}. \quad (\text{B3})$$

For hole doping with density n_h , the result for its Fermi energy E_F^h is quite similar, except that $c_1^{(2)} < 0$ and the upper valence subband edge sits at $\mathbb{E} = -\Delta/2 + \lambda_0$. This yields

$$E_F^h = \frac{1}{c_1^{(2)}} \left\{ -c_0^{(2)} + \left\{ -2n_h c_1^{(2)} + \left[c_0^{(2)} - c_1^{(2)} \left(\frac{\Delta}{2} - \lambda_0 \right) \right]^2 \right\}^{1/2} \right\}. \quad (\text{B4})$$

Using the above expression, we can further improve the result in Eq. (B1) for the critical hole doping density n_c^h required to populate the lower subband at $T = 0$. In such a case, we have $E_F^h = -\Delta/2 - \lambda_0$ and $n_c^h = -\lambda_0 \Delta c_1^{(2)} + 2c_0^{(2)} \lambda_0 = 3.3 \times 10^{13} \text{ cm}^{-2}$. This critical density is still far above the experimentally accessible value $\simeq 1.0 \times 10^{13} \text{ cm}^{-2}$. Therefore, we will assume the lower hole subband is unpopulated at $T = 0$ for all our calculations.

We now turn to deriving a set of explicit equations for $\mu(T)$ of MoS₂. Our derivation is based on the total carrier density conservation and includes thermally-excited electrons and holes, yielding⁷³

$$n = n_e(T) - n_h(T) = \int_0^\infty d\mathbb{E} \rho_d(\mathbb{E}) f_{\gamma=1}(\mathbb{E}, T) - \int_{-\infty}^0 d\mathbb{E} \rho_d(\mathbb{E}) \{1 - f_{\gamma=1}(\mathbb{E}, T)\}. \quad (\text{B5})$$

Here, the electron and hole occupation probabilities are complimentary, and the hole term does not play a role in Eq. (B5) for electron doping (see Ref. [109] for details).

Mathematically, Eq. (B5) can be formally rewritten as $n = \mathcal{I}_e(\Delta|T) - \mathcal{I}_h(\Delta, \lambda_0|T)$. For further simplifying calculations, we introduce the following two auxiliary functions

$$\begin{aligned} \mathcal{A}_0(\mathbb{E}, T) &= \left\{ 1 + \exp \left[\frac{\mathbb{E} - \mu(T)}{k_B T} \right] \right\}^{-1}, \\ \mathcal{A}_1(\mathbb{E}, T) &= \mathbb{E} \mathcal{A}^{(0)}(\mathbb{E}, T) = \mathbb{E} \left\{ 1 + \exp \left[\frac{\mathbb{E} - \mu(T)}{k_B T} \right] \right\}^{-1}. \end{aligned} \quad (\text{B6})$$

As a result, we can write

$$\mathcal{I}_e(\Delta|T) = \sum_{j=0}^1 c_j^{(3)} \int_{\Delta/2}^\infty d\mathbb{E} \mathcal{A}_j(\mathbb{E}, T). \quad (\text{B7})$$

By introducing a variable substitution $\xi = (\mathbb{E} - \Delta_<)/k_B T$ and the following notation

$$\mathcal{R}_p(T, X) = \int_0^\infty d\xi \xi^p \{1 + \exp[\xi - X/(k_B T)]\}^{-1}, \quad (\text{B8})$$

$\mathcal{I}_e(\Delta|T)$ can be explicitly calculated as

$$\mathcal{I}_e(\Delta|T) = k_B T \left(c_0^{(3)} + \frac{\Delta}{2} \right) \mathcal{R}_0(T, \mu(T) - \Delta/2) + c_1^{(3)} (k_B T)^2 \mathcal{R}_1(T, \mu(T) - \Delta/2) , \quad (\text{B9})$$

where the two terms with $p = 0, 1$ correspond to a 2DEG and gapless graphene. After a simple computation, Eq. (B8) turns into^{89,90}

$$\begin{aligned} \mathcal{R}_0(T, X) &= \ln \left\{ 1 + \exp \left[\frac{X}{k_B T} \right] \right\} , \\ \mathcal{R}_1(T, X) &= -\text{Li}_2 \left\{ -\exp \left[\frac{X}{k_B T} \right] \right\} , \end{aligned} \quad (\text{B10})$$

where $\text{Li}_2(z)$ is the second-order polylogarithm function or dilogarithm, defined by

$$\text{Li}_2(z) = - \int_0^z \frac{\ln(1-t)}{t} dt . \quad (\text{B11})$$

In a similar way, the hole term introduced in Eq. (B5) can be expressed as

$$\begin{aligned} \int_{-\infty}^0 d\mathbb{E} \rho_d(|\mathbb{E}|) \{1 - f_1(\mathbb{E}, T)\} &= \int_{-\infty}^{-\Delta/2+\lambda_0} d\mathbb{E} \left[-c_1^{(2)} \mathbb{E} + c_0^{(2)} \right] \left\{ 1 + \exp \left[\frac{\mu(T) - \mathbb{E}}{k_B T} \right] \right\}^{-1} \\ &+ \int_{-\infty}^{-\Delta/2-\lambda_0} d\mathbb{E} \left[-\delta c_1^{(1)} \mathbb{E} + \delta c_0^{(1)} \right] \left\{ 1 + \exp \left[\frac{\mu(T) - \mathbb{E}}{k_B T} \right] \right\}^{-1} = \sum_{j=1}^4 \mathcal{I}_h^{(j)}(\Delta, \lambda_0|T) , \end{aligned} \quad (\text{B12})$$

where $\delta c_i^{(1)} = c_i^{(1)} - c_i^{(2)}$ for $i = 0, 1$, and

$$\begin{aligned} \mathcal{I}_h^{(1)}(\Delta, \lambda_0|T) &= k_B T \left(\frac{\Delta}{2} - \lambda_0 + c_2^{(0)} \right) \mathcal{R}_0(T, -[\mu(T) + \Delta/2 - \lambda_0]) , \\ \mathcal{I}_h^{(2)}(\Delta, \lambda_0|T) &= c_2^{(1)} (k_B T)^2 \mathcal{R}_1(T, -[\mu(T) + \Delta/2 - \lambda_0]) , \\ \mathcal{I}_h^{(3)}(\Delta, \lambda_0|T) &= k_B T \left(\frac{\Delta}{2} + \lambda_0 + \delta c_1^{(0)} \right) \mathcal{R}_0(T, -[\mu(T) + \Delta/2 + \lambda_0]) , \\ \mathcal{I}_h^{(4)}(\Delta, \lambda_0|T) &= \delta c_1^{(1)} (k_B T)^2 \mathcal{R}_1(T, -[\mu(T) + \Delta/2 + \lambda_0]) . \end{aligned} \quad (\text{B13})$$

Combined with the electron terms in Eq. (B9), these hole terms in Eq. (B13) give the right-hand side of Eq (B5). The left-hand side of Eq (B5) is given by Eq. (B2) for electron doping and for hole doping by

$$n_h = \left(\frac{\Delta}{2} + E_F^h - \lambda_0 \right) \left\{ c_0^{(2)} + \frac{c_1^{(2)}}{2} \left[\frac{\Delta}{2} - (E_F^h + \lambda_0) \right] \right\} . \quad (\text{B14})$$

It is evident that the symmetry between electron and hole states no longer holds, which strongly affects the finite T behavior of $\mu(T)$ in MoS₂.

$\mu(T)$ for buckled honeycomb lattices

The DOS of silicene is given by Eq. (5). The expression for E_F^e at $T = 0$ with a fixed n_e depends on whether one or both electron subbands are populated. For the former case, we require

$$n_e \leq n_c = \frac{1}{2\pi} \frac{\Delta_>^2 - \Delta_<^2}{\hbar^2 v_F^2} = \frac{2}{\pi \hbar^2 v_F^2} \Delta_{SO} \Delta_z , \quad (\text{B15})$$

and E_F^e is obtained from

$$n_e = \frac{1}{2\pi} \frac{(E_F^e)^2 - \Delta_<^2}{\hbar^2 v_F^2} . \quad (\text{B16})$$

Alternatively, if both subbands are populated, E_F^e is determined by

$$n_e = \frac{1}{\pi} \frac{1}{\hbar^2 v_F^2} \left[(E_F^e)^2 - \frac{1}{2} (\Delta_<^2 + \Delta_>^2) \right] . \quad (\text{B17})$$

At finite T , we once again use the conservation of the carrier density in Eq. (B5). In this case, $\mu(T)$ of silicene is easily obtained as a limiting case of our derivation above

$$n_e = \left(\frac{k_B T}{\hbar v_F} \right)^2 \sum_{\gamma=\pm 1} \frac{\gamma}{\pi} \sum_{i=<,>} \mathcal{R}_1(T, \gamma\mu(T) - \Delta_i) + \frac{\Delta_i}{k_B T} \mathcal{R}_0(T, \gamma\mu(T) - \Delta_i) . \quad (\text{B18})$$

Using the polylogarithm functions, we can explicitly write

$$n_e \left(\frac{\hbar v_F}{k_B T} \right)^2 = \sum_{\gamma=\pm 1} \frac{\gamma}{\pi} \sum_{i=<,>} -\text{Li}_2 \left\{ -\exp \left[\frac{\gamma\mu(T) - \Delta_i}{k_B T} \right] \right\} + \frac{\Delta_i}{k_B T} \ln \left\{ 1 + \exp \left[\frac{\gamma\mu(T) - \Delta_i}{k_B T} \right] \right\} . \quad (\text{B19})$$

As a special example, $\mu(T)$ for gapped graphene with two fourfold degenerate energy subbands can be obtained by setting $\Delta_< = \Delta_> = \Delta_0$ and $\sum_{i=<,>} \implies 2$. Moreover, for gapless graphene, we have $\Delta_0 = 0$ and $\pi n_e = [E_F^e / (\hbar v_F)]^2$.

As a result, we find

$$\frac{(E_F^e)^2}{2(k_B T)^2} = \sum_{\gamma=\pm 1} \gamma \mathcal{R}_1(T, \gamma\mu(T)) = - \sum_{\gamma=\pm 1} \gamma \text{Li}_2 \left\{ -\exp \left[\frac{\gamma\mu(T)}{k_B T} \right] \right\} . \quad (\text{B20})$$

If $k_B T \ll E_F^e$ is satisfied, the above result is simplified to⁷³

$$\mathcal{R}_1(T, \gamma\mu(T)) \simeq \left(\frac{Y^2}{2} + \frac{\pi^2}{6} \right) \Theta(Y) + Y \ln \left(1 + e^{-|Y|} \right) , \quad (\text{B21})$$

where $Y = \gamma\mu(T)/k_B T$.

At last, we would briefly address the case of hole doping with $E_F^h < 0$. In this case, the left-hand part of Eq. (B5) takes the form

$$-n_h = -\frac{2}{\pi} \frac{1}{(\hbar v_F)^2} \sum_{i=<,>} \int_{-\infty}^{-\Delta_i} d\mathbb{E} |\mathbb{E}| \Theta(-\mathbb{E} + E_F^h) . \quad (\text{B22})$$

In analogy with electron doping, E_F^h depends on whether only the $\Delta_<$ -subband (which is the higher one now) or both subbands are occupied. The equations for determining E_F^h for a given n_h are the same as Eqs. (B16) and (B17), which confirms a complete symmetry between electron and hole states in silicene. The right-hand side of Eq. (B5) remains unchanged except for $\mu(T) < 0$ at a finite T .

¹ T. Ando, A. B. Fowler, and F. Stern, Reviews of Modern Physics **54**, 437 (1982).

- ² F. Stern, Phys. Rev. Lett. **18**, 546 (1967).
- ³ K. Novoselov, A. K. Geim, S. Morozov, D. Jiang, M. Katsnelson, I. Grigorieva, S. Dubonos, and A. Firsov, nature **438**, 197 (2005).
- ⁴ A. K. Geim and K. S. Novoselov, Nature materials **6**, 183 (2007).
- ⁵ A. C. Neto, F. Guinea, N. Peres, K. S. Novoselov, and A. K. Geim, Reviews of modern physics **81**, 109 (2009).
- ⁶ A. C. Neto, F. Guinea, N. M. Peres, K. S. Novoselov, and A. K. Geim, Reviews of modern physics **81**, 109 (2009).
- ⁷ P. Avouris, Nano letters **10**, 4285 (2010).
- ⁸ H.-R. Chang, J. Zhou, H. Zhang, and Y. Yao, Phys. Rev. B **89**, 201411 (2014).
- ⁹ G. Giovannetti, P. A. Khomyakov, G. Brocks, P. J. Kelly, and J. van den Brink, Physical Review B **76**, 073103 (2007).
- ¹⁰ N. Kharche and S. K. Nayak, Nano letters **11**, 5274 (2011).
- ¹¹ Z. H. Ni, T. Yu, Y. H. Lu, Y. Y. Wang, Y. P. Feng, and Z. X. Shen, ACS nano **2**, 2301 (2008).
- ¹² O. Kibis, Physical Review B **81**, 165433 (2010).
- ¹³ X. Li, X. Wang, L. Zhang, S. Lee, and H. Dai, science **319**, 1229 (2008).
- ¹⁴ Y.-W. Son, M. L. Cohen, and S. G. Louie, Physical review letters **97**, 216803 (2006).
- ¹⁵ M. Y. Han, B. Özyilmaz, Y. Zhang, and P. Kim, Physical review letters **98**, 206805 (2007).
- ¹⁶ M. Ezawa, New Journal of Physics **14**, 033003 (2012).
- ¹⁷ C. J. Tabert and E. J. Nicol, Phys. Rev. B **89**, 195410 (2014).
- ¹⁸ B. Lalmi, H. Oughaddou, H. Enriquez, A. Kara, S. Vizzini, B. Ealet, and B. Aufray, Applied Physics Letters **97**, 223109 (2010).
- ¹⁹ C. L. Kane and E. J. Mele, Phys. Rev. Lett. **95**, 226801 (2005).
- ²⁰ M. Ezawa, Phys. Rev. Lett. **109**, 055502 (2012).
- ²¹ N. D. Drummond, V. Zólyomi, and V. I. Fal'ko, Phys. Rev. B **85**, 075423 (2012).
- ²² B. Aufray, A. Kara, S. Vizzini, H. Oughaddou, C. Leandri, B. Ealet, and G. Le Lay, Applied Physics Letters **96**, 183102 (2010).
- ²³ P. De Padova, C. Quaresima, C. Ottaviani, P. M. Sheverdyaeva, P. Moras, C. Carbone, D. Topwal, B. Olivieri, A. Kara, H. Oughaddou, et al., Applied Physics Letters **96**, 261905 (2010).
- ²⁴ L. Zhang, P. Bampoulis, A. van Houselt, and H. Zandvliet, Applied Physics Letters **107**, 111605 (2015).
- ²⁵ A. Acun, L. Zhang, P. Bampoulis, M. Farmanbar, A. van Houselt, A. Rudenko, M. Lingenfelder, G. Brocks, B. Poelsema, M. Katsnelson, et al., Journal of Physics: Condensed Matter **27**, 443002 (2015).
- ²⁶ L. Li, S.-z. Lu, J. Pan, Z. Qin, Y.-q. Wang, Y. Wang, G.-y. Cao, S. Du, and H.-J. Gao, Advanced Materials **26**, 4820 (2014).
- ²⁷ M. Dávila, L. Xian, S. Cahangirov, A. Rubio, and G. Le Lay, New Journal of Physics **16**, 095002 (2014).
- ²⁸ P. Bampoulis, L. Zhang, A. Safaei, R. Van Gastel, B. Poelsema, and H. J. W. Zandvliet, Journal of physics: Condensed matter **26**, 442001 (2014).
- ²⁹ M. Derivaz, D. Dentel, R. Stephan, M.-C. Hanf, A. Mehdaoui, P. Sonnet, and C. Pirri, Nano letters **15**, 2510 (2015).
- ³⁰ F. dAcapito, S. Torrenço, E. Xenogiannopoulou, P. Tsipas, J. M. Velasco, D. Tsoutsou, and A. Dimoulas, Journal of Physics: Condensed Matter **28**, 045002 (2016).
- ³¹ R. Ganatra and Q. Zhang, ACS nano **8**, 4074 (2014).
- ³² H. Rostami, A. G. Moghaddam, and R. Asgari, Physical Review B **88**, 085440 (2013).
- ³³ K. Kośmider, J. W. González, and J. Fernández-Rossier, Phys. Rev. B **88**, 245436 (2013).
- ³⁴ D. Xiao, G.-B. Liu, W. Feng, X. Xu, and W. Yao, Phys. Rev. Lett. **108**, 196802 (2012).
- ³⁵ A. Kormányos, V. Zólyomi, N. D. Drummond, P. Rakya, G. Burkard, and V. I. Fal'ko, Phys. Rev. B **88**, 045416 (2013).
- ³⁶ H. Rostami, R. Roldán, E. Cappelluti, R. Asgari, and F. Guinea, Physical Review B **92**, 195402 (2015).
- ³⁷ B. Radisavljevic, A. Radenovic, J. Brivio, i. V. Giacometti, and A. Kis, Nature nanotechnology **6**, 147 (2011).
- ³⁸ A. Scholz, T. Stauber, and J. Schliemann, Phys. Rev. B **88**, 035135 (2013).
- ³⁹ L. Wang, A. Kutana, and B. I. Yakobson, Annalen der Physik **526** (2014).
- ⁴⁰ O. Kibis, K. Dini, I. Iorsh, and I. Shelykh, Physical Review B **95**, 125401 (2017).
- ⁴¹ G. Giuliani and G. Vignale, *Quantum theory of the electron liquid* (Cambridge university press, 2005).
- ⁴² G. Gumbs and D. Huang, *Properties of Interacting Low-Dimensional Systems* (John Wiley & Sons, 2013).
- ⁴³ C. J. Tabert and E. J. Nicol, Physical review letters **110**, 197402 (2013).
- ⁴⁴ C. J. Tabert and E. J. Nicol, Physical Review B **87**, 235426 (2013).
- ⁴⁵ C. J. Tabert and E. J. Nicol, Physical Review B **88**, 085434 (2013).
- ⁴⁶ T. Ando, Journal of the Physical Society of Japan **75**, 074716 (2006).
- ⁴⁷ P. Pyatkovskiy, Journal of Physics: Condensed Matter **21**, 025506 (2008).
- ⁴⁸ S. D. Sarma, E. Hwang, and H. Min, Physical Review B **91**, 035201 (2015).
- ⁴⁹ O. Sobol, P. Pyatkovskiy, E. Gorbar, and V. Gusynin, Physical Review B **94**, 115409 (2016).
- ⁵⁰ B. Wunsch, T. Stauber, F. Sols, and F. Guinea, New Journal of Physics **8**, 318 (2006).
- ⁵¹ E. H. Hwang and S. Das Sarma, Phys. Rev. B **75**, 205418 (2007).
- ⁵² S. Das Sarma and Q. Li, Phys. Rev. B **87**, 235418 (2013).
- ⁵³ T. Stauber, J. Schliemann, and N. M. R. Peres, Phys. Rev. B **81**, 085409 (2010).
- ⁵⁴ A. Scholz, T. Stauber, and J. Schliemann, Phys. Rev. B **86**, 195424 (2012).
- ⁵⁵ T. Stauber, G. Gómez-Santos, and L. Brey, arXiv preprint arXiv:1706.09403 (2017).
- ⁵⁶ S. Das Sarma and E. H. Hwang, Phys. Rev. Lett. **102**, 206412 (2009).
- ⁵⁷ H. Yan, T. Low, W. Zhu, Y. Wu, M. Freitag, X. Li, F. Guinea, P. Avouris, and F. Xia, Nature Photonics **7**, 394 (2013).

- ⁵⁸ J. Chen, M. Badioli, P. Alonso-González, S. Thongrattanasiri, F. Huth, J. Osmond, M. Spasenović, A. Centeno, A. Pesquera, P. Godignon, et al., *Nature* **487**, 77 (2012).
- ⁵⁹ X. Luo, T. Qiu, W. Lu, and Z. Ni, *Materials Science and Engineering: R: Reports* **74**, 351 (2013).
- ⁶⁰ A. Grigorenko, M. Polini, and K. Novoselov, *Nature photonics* **6**, 749 (2012).
- ⁶¹ J. H. Strait, P. Nene, W.-M. Chan, C. Manolatou, S. Tiwari, F. Rana, J. W. Kevek, and P. L. McEuen, *Physical Review B* **87**, 241410 (2013).
- ⁶² G. Gumbs, A. Iurov, D. Huang, and W. Pan, *Journal of Applied Physics* **118**, 054303 (2015).
- ⁶³ A. Politano and G. Chiarello, *Nanoscale* **6**, 10927 (2014).
- ⁶⁴ A. Politano, V. M. Silkin, I. A. Nechaev, M. S. Vitiello, L. Viti, Z. S. Aliev, M. B. Babanly, G. Chiarello, P. M. Echenique, and E. V. Chulkov, *Phys. Rev. Lett.* **115**, 216802 (2015).
- ⁶⁵ A. Politano, A. R. Marino, V. Formoso, D. Fariás, R. Miranda, and G. Chiarello, *Phys. Rev. B* **84**, 033401 (2011).
- ⁶⁶ A. Politano, A. R. Marino, and G. Chiarello, *Phys. Rev. B* **86**, 085420 (2012).
- ⁶⁷ A. Politano and G. Chiarello, *Applied Physics Letters* **102**, 201608 (2013).
- ⁶⁸ A. Politano and G. Chiarello, *2D Materials* **4**, 035003 (2017).
- ⁶⁹ A. Politano, I. Radović, D. Borka, Z. Mišković, H. Yu, D. Farias, and G. Chiarello, *Carbon* **114**, 70 (2017).
- ⁷⁰ S. Das Sarma and Q. Li, *Phys. Rev. B* **87**, 235418 (2013).
- ⁷¹ D. K. Patel, S. S. Ashraf, and A. C. Sharma, *physica status solidi (b)* **252**, 1817 (2015).
- ⁷² J. Wu, S. Chen, and M. Lin, *New Journal of Physics* **16**, 125002 (2014).
- ⁷³ E. H. Hwang and S. Das Sarma, *Phys. Rev. B* **79**, 165404 (2009).
- ⁷⁴ L. Meng, Y. Zhang, W. Yan, L. Feng, L. He, R.-F. Dou, and J.-C. Nie, *Applied Physics Letters* **100**, 091601 (2012).
- ⁷⁵ P. Plochocka, C. Faugeras, M. Orlita, M. L. Sadowski, G. Martinez, M. Potemski, M. O. Goerbig, J.-N. Fuchs, C. Berger, and W. A. De Heer, *Physical review letters* **100**, 087401 (2008).
- ⁷⁶ M. Pizarra, A. Sindona, P. Riccardi, V. Silkin, and J. Pitarke, *New Journal of Physics* **16**, 083003 (2014).
- ⁷⁷ V. Despoja, D. Novko, K. Dekanić, M. Šunjić, and L. Marušić, *Physical Review B* **87**, 075447 (2013).
- ⁷⁸ C. Vacacela Gomez, M. Pizarra, M. Gravina, P. Riccardi, and A. Sindona, *Phys. Rev. B* **95**, 085419 (2017).
- ⁷⁹ D. Novko, *Nano Letters* (2017).
- ⁸⁰ M. Jablan, H. Buljan, and M. Soljačić, *Physical review B* **80**, 245435 (2009).
- ⁸¹ E. Hwang and S. D. Sarma, *Physical Review B* **77**, 115449 (2008).
- ⁸² T. Stauber, N. Peres, and F. Guinea, *Physical Review B* **76**, 205423 (2007).
- ⁸³ A. Woessner, M. B. Lundberg, Y. Gao, A. Principi, P. Alonso-González, M. Carrega, K. Watanabe, T. Taniguchi, G. Vignale, M. Polini, et al., *Nature materials* **14**, 421 (2015).
- ⁸⁴ P. F. Maldague, *Surface Science* **73**, 296 (1978).
- ⁸⁵ A. Iurov, G. Gumbs, and D. Huang, *Journal of Physics: Condensed Matter* **29**, 135602 (2017).
- ⁸⁶ C. Walhout, A. Acun, L. Zhang, M. Ezawa, and H. Zandvliet, *Journal of physics: Condensed matter* **28**, 284006 (2016).
- ⁸⁷ E. V. Gorbar, V. P. Gusynin, V. A. Miransky, and I. A. Shovkovy, *Phys. Rev. B* **66**, 045108 (2002).
- ⁸⁸ V. Y. Tsaran, A. Kavokin, S. Sharapov, A. Varlamov, and V. Gusynin, *arXiv preprint arXiv:1703.08962* (2017).
- ⁸⁹ E. W. Weisstein, *CRC concise encyclopedia of mathematics* (CRC press, 2002).
- ⁹⁰ I. S. Gradshteyn and I. M. Ryzhik, *Table of integrals, series, and products* (Academic press, 2014).
- ⁹¹ A. Iurov, G. Gumbs, D. Huang, and V. Silkin, *Physical Review B* **93**, 035404 (2016).
- ⁹² A. Iurov, G. Gumbs, D. Huang, and L. Zhemchuzhna, *Journal of Applied Physics* **121**, 084306 (2017).
- ⁹³ D. Xiao, G.-B. Liu, W. Feng, X. Xu, and W. Yao, *Physical Review Letters* **108**, 196802 (2012).
- ⁹⁴ Y. Gogotsi and V. Presser, *Carbon nanomaterials* (CRC press, 2013).
- ⁹⁵ H. Raza, *Graphene nanoelectronics: metrology, synthesis, properties and applications* (Springer Science & Business Media, 2012).
- ⁹⁶ W. L. Barnes, A. Dereux, and T. W. Ebbesen, *Nature* **424**, 824 (2003).
- ⁹⁷ G. Gumbs, A. Iurov, and N. J. M. Horing, *Phys. Rev. B* **91**, 235416 (2015).
- ⁹⁸ M. Campisi, P. Hänggi, and P. Talkner, *Rev. Mod. Phys.* **83**, 771 (2011).
- ⁹⁹ G. Schaller, *Open quantum systems far from equilibrium*, vol. 881 (Springer, 2014).
- ¹⁰⁰ N. J. Horing, A. Iurov, G. Gumbs, A. Politano, and G. Chiarello, in *Low-Dimensional and Nanostructured Materials and Devices* (Springer, 2016), pp. 205–237.
- ¹⁰¹ N. J. M. Horing, *Physical Review B* **80**, 193401 (2009).
- ¹⁰² N. J. M. Horing, *Philosophical Transactions of the Royal Society of London A: Mathematical, Physical and Engineering Sciences* **368**, 5525 (2010).
- ¹⁰³ N. J. M. Horing, E. Kamen, and H.-L. Cui, *Physical Review B* **32**, 2184 (1985).
- ¹⁰⁴ G. Gumbs, A. Iurov, J.-Y. Wu, M. Lin, and P. Fekete, *Scientific reports* **6** (2016).
- ¹⁰⁵ C. Kramberger, R. Hambach, C. Giorgetti, M. H. Rummeli, M. Knupfer, J. Fink, B. Büchner, L. Reining, E. Einarsson, S. Maruyama, et al., *Phys. Rev. Lett.* **100**, 196803 (2008).
- ¹⁰⁶ E. d. A. e Silva, G. La Rocca, and F. Bassani, *Physical Review B* **55**, 16293 (1997).
- ¹⁰⁷ M. Burt, *Semiconductor science and technology* **3**, 739 (1988).
- ¹⁰⁸ M. Ezawa, *Applied Physics Letters* **102**, 172103 (2013).
- ¹⁰⁹ T. Izraeli, *Final Project in the Computational Physics Course* (2013).
- ¹¹⁰ Expression $k_F = \sqrt{\pi n}$ holds true only for systems with a fourfold spin and valley degeneracy, such as graphene, i.e., $g = g_s g_v = 4$. However, the general relation between doping density n and k_F in a 2D material is $(2\pi)^2 n = g \pi k_F^2$.
- ¹¹¹ Due to a large gap parameter $\Delta = 1.9 eV$, the electronic states corresponding to large wave vectors are required to be taken

into account. As $k \approx 5.0 k_0$, we find the correction $\simeq \beta \Delta k^4$ from our exact numerical result becomes no longer negligible.